Department of Experimental Physics

Faculty of Science

PALACKY UNIVERSITY, OLOMOUC

Composites of two-dimensional materials for energy storage

Doctoral Dissertation

By

Smita Talande, MSc

Under

Study program P1703 Physics

Supervisor: Aristeidis Bakandritsos, Ph.D.

Olomouc, 2020

Annotation

Department of Experimental Physics, Faculty of Science

Palacky University, Olomouc

Candidate	Smita Talande, MSc
Supervisor	Aristeidis Bakandritsos, Ph.D.
Co-supervisors	Jiří Tuček, Ph.D. and Manoj B. Gawande, Ph.D.
Number of pages	88
Number of attachments	2
Year	2020
Abstract	The constant increase in energy demand combined with our non-renewable fossil fuel-based civilization producing a negative environmental impact (CO_2 emission) calls for the development of sustainable energy conversion and storage with a small environmental footprint. Electrochemical technologies such as supercapacitors (SCs) and batteries are emerging as important energy storage devices for electronics, electric vehicles, and smart grids. SCs display remarkable advantages over batteries, such as ultrafast charging, high power dissipation, and extra-long cycle-life. Furthermore, they are a cheaper and far more sustainable energy storage technology, since they are carbon-based, not requiring low-abundance elements as batteries do (*i.e.* lithium, cobalt, or nickel). However, state-of-the-art SCs materials are lagging behind Li-ion batteries in energy content by order of magnitude. A lot of research effort is thus focused on increasing the energy content of SCs in order to exploit their advantages in applications requiring energy supply for more extended periods. For this purpose, we have studied methods in order to increase the performance of SCs electrode materials *via* developing hybrids by combining the densely functionalized graphene derivative (Cyanographene, GCN) with ultra-small nanoparticles of β-FeOOH and Fe_3S_4.
Keywords	Supercapacitors, transition metal oxides/ sulfides, functionalized graphene, non-aqueous electrolyte, energy density

Declaration of the Author

I at this moment declare that this dissertation entitled "Composites of two-dimensional materials for energy storage" is my original work performed during my doctoral study and I have written it under the supervision of Aristeidis Bakandritsos, PhD. All experimental work is carried out in the RCPTM, Olomouc. The additional information used for the completion of the work is appropriately acknowledged in the references. I declare that this dissertation is not submitted elsewhere to obtain any academic degree.

In Olomouc, 11 November 2020 ……

Smita Talande M.Sc.

Acknowledgement

I would like to thank Dr. Aristeidis Bakandritsos, my supervisor, for his guidance, valuable advice and constructive suggestions during my doctoral studies. Also Assoc. Prof. Jiri Tucek and Dr Manoj Gawande for their helpful guidance and help throughout my doctoral studies.

Further, I am thankful to Dr. Petr Jakubec for his tutoring in electrochemical impedance spectroscopy and Dr. Ondrej Malina for the Mossbaure measurements and analysis. I also thank my collogues who helped me for the characterization, Jana Stráská (TEM), Dr. Claudia Aparicio and Dr. Josef Kašlík (XRD), Dr. Juri Ugolotti and Jana Havláková (TGA and EGA), Martin Petr (XPS), and Mgr. Tomáš Steklý (cyanographene preparation).

I would extend my thanks to everyone with whom I collaborated during my doctoral studies. I am grateful to Prof. Volker Presser, Prof. Michal Otyepka and Prof. Radek Zboril, for their constructive comments and suggestions for my first author publications.

I would express my gratitude to my family and friends for their generous support and motivation during my studies.

Finally, I would gratefully acknowledge the financial support by J. L. Fischer scholarship and IGA grants of Palacký University (IGA_PrF_2019_023 and IGA_PrF_2020_011).

Dedicated to

My parents and beloved husband

Table of Contents

CHAPTER 1

INTRODUCTION TO ENERGY STORAGE

1.1 Introduction

The intensive consumption of fossil fuels leads to profound release of greenhouse gases with a detrimental environmental impact. Therefore, the development of alternative strategies for energy production and management is becoming more and more critical for securing a sustainable future. During the last decades, sustainable and renewable energy resources, such as wind and solar power, are developing at high pace. Although sun and wind can produce a large amount of energy, production depends on the weather conditions, and thus is largely uncontrolled. Thus, the peak time of energy production may not coincide with the energy demand, and vice versa. For this reason, it is of key importance to be able to store the surplus of produced energy whenever it is available, and provide it later or elsewhere, when and where there is energy demand. In addition, due to the rapid development of mobile electronics for communication, processing, and accessing information, for remote networking and device co-operation for the internet-of-things, there is a growing demand for portable power. [1–3]Thus, the development of effective energy storage system/devices, with improved performance and safety fabricated from sustainable resources has aroused intense research interest and efforts.

1.2 Energy storage systems

To date, pumped hydropower is dominating the energy storage landscape worldwide. Compressed air, thermal energy storage and electrochemical energy storage (EES) are also being widely applied. However, only EES systems are modular and can be used both for stationary and portable energy storage. The EES systems store energy in electrochemical (or electrostatic) form during the

charging process, and *via* discharging this form of energy is released back in electric form. Besides, EES systems (*e.g.* batteries and supercapacitors) are suitable for sensitive electronic devices and circuits, since the flow of power can be controlled.[4] However, current EES systems require significant advancements in order to become more efficient (faster charging/discharging and with higher energy content) for application in electric vehicles, to increase their life-cycle for more reliable utilization in electronic devices, as well as to shift their fabrication to more sustainable and earth abundant components.

1.3 Batteries and Supercapacitors

At present, the EES systems have been developed in various types based on their working principle. Supercapacitors[4] store charges by the formation of an electrochemical double layer (EDL) and/or surface redox reactions. Batteries (such as lead-acid, lithium-ion, sodium-sulfur), flow batteries (for *e.g.* vanadium redox flow batteries) store charges through the (faradic) redox reactions undergoing in bulk of the electrode materials. Batteries are being widely applied and further developed because of their ability to store a lot of energy. Thus, they are already applied in hybrid/electric vehicles, laptops, mobile phones, and several other portable electronic devices. Nevertheless, they suffer from a gradual decrease in performance upon charging/discharging, while their rate performance i.e. the rate of charging and discharging is low.[5] Batteries are mainly classified into two types, namely primary and secondary (or rechargeable) batteries. The primary batteries (or dry cells) undergoes through irreversible redox reactions thus can be used only once. Such batteries are used in small portable devices (such as wristwatches, calculators, torches).

On the other hand, rechargeable batteries undergo reversible redox reactions thus can be charge-discharge several times and can be further classified into two types based on their cell

design. The standard cell design, in which all required materials and electrolyte are enclosed in a single cell and are widely used in portable devices. The second type is flow-battery whereby electrolytes are stored in separate containers outside the cell and pumped into the electrochemical cell when needed. Because of this, the battery capacity can be enhanced by increasing the electrolyte's container size,[5] thus are suitable for power grid application where large capacities are most important and space is not that important issue.

The *lead-acid battery* is the very first rechargeable battery, developed by Gaston Plante in the year 1859, and still used in some applications (for example cars). This battery is assembled with lead (Pb) as a negative electrode, and lead peroxide (PbO_2) as a positive electrode immersed in sulfuric acid (H_2SO_4) used as an electrolyte. In the discharging process, the negative electrode (*i.e.* Pb) and H_2SO_4 undergo oxidation reaction to form lead sulfate ($PbSO_4$) and releases hydrogen ions. Meanwhile, electrons flow through an external circuit to the positive electrode, *i.e.* PbO_2, where they take part in the reduction reaction to form $PbSO_4$ and H_2O.[5] The total reaction can be written as:

$$Pb + PbO_2 + 2H_2SO_4 \rightarrow 2PbSO_4 + 2H_2O \qquad (l.1)$$

Thus, both electrodes are converted into lead sulfate during discharging. While charging, the reverse reactions take place on both electrodes. At the negative electrode, the lead sulfate is converted back into lead, and at the positive electrode, the lead sulfate is converted back into lead peroxide [6]

The *Nickel-cadmium battery* was invented back in 1899 by Waldemar Jungner, and it is the most developed battery type compared to other nickel batteries, such as nickel-metal hydride, nickel-iron or nickel-zinc battery. Nickel-cadmium battery has high energy density (*E*), and it is

lightweight compared to the lead-acid batteries. However, they suffer from memory effect as well they quickly self-discharge compared to lead-acid batteries.[5]

The *lithium-ion battery* (LIB) is widely applied in portable electronic devices (mobile phones, laptops) as well as in electric vehicles, because of its high energy density, long lifetime compared to other battery types and the low density of Lithium (Li). Also, it has very-low self-discharge and minimal memory effect.[5]

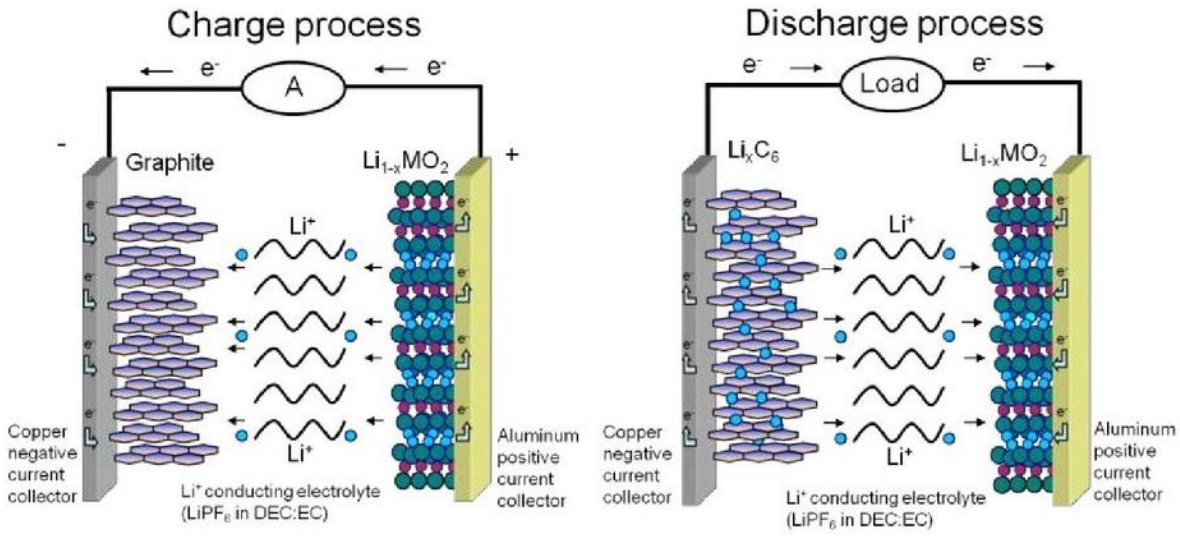

Figure 1.1. Working principle of Li-ion battery. (ref.[7])

The working principle of LIB is based on the reaction between metallic lithium (Li) and metal oxide (MO_2). The negative and positive electrodes are mostly graphite and Li-embedded metal oxide, respectively. During charging, Li-ions are formed at positive electrode (cathode) travel to the negative electrode (anode) through an electrolyte and intercalate into graphite. Whereas, during discharging, these Li-ions travel back to the positive electrode (**Figure 1.1**). The reaction is as follows (considering $LiCoO_2$ as a cathode):

At anode, $C_6Li_x \rightarrow 6\ C\ (graphite) + xLi^+ + xe^-$ (1.2)

At cathode, $Li_{1-x}CoO_2 + xLi^+ + xe^- \rightarrow LiCoO_2$ (1.3)

Total reaction is, $LiCoO_2 + 6\,C \rightarrow Li_{1-x}CoO_2 + C_6Li_x$ (1.4)

Supercapacitors (SCs), are the electrochemical capacitors, which possess high energy densities compared to dielectric capacitors, and possess high-power density (*P*) compared to the batteries **(Figure 1.2)**. Thus, also known as a bridging device between dielectric capacitors and batteries.[8]

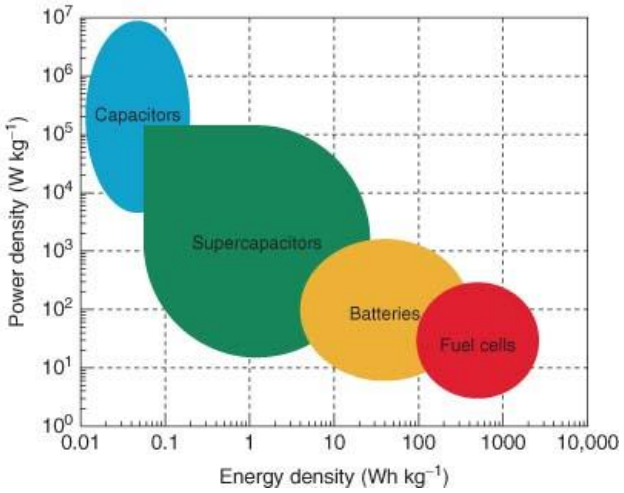

Figure 1.2 Energy and power densities representation of electrochemical energy storage and conversion devices. (Ref.[9])

The double-layer supercapacitor was first developed and patented by Becker in 1957, using porous carbon as the electrode material and sulfuric acid as an electrolyte. Mainly, SCs store charges based on electrostatic absorption mechanism, and due to this simple charge storage mechanism, the SCs have long lifetime compared to batteries.[9,10] Moreover, SCs are considered as an effective storage device and are intensively studied and developed because of their fast charge-discharge ability, high power density and, longer lifetime than batteries. However, their low energy content hinders the practical application of SCs in several, energy-demanding devices/applications such as electric vehicles. Thus, it is crucial to increase the energy density of SCs.

CHAPTER 2

SUPERCAPACITORS

2.1 Introduction to supercapacitors

Batteries and supercapacitors are attractive energy storage devices due to their portable, fast storage capacity and their high energy (batteries) and high power (SCs). Li-ion batteries can provide high energy density (~ 180 Wh kg^{-1}). Although, heat generation (as a result of sluggish kinetics), and dendrites formation when operated at high power or for the long time, poses safety issues.[11] On the other hand, SCs, which have simple charge storage mechanism assures safety during operation even during charging with high currents. **Figure 2.1** shows the energy and power that can be achieved by using various types of batteries, and SCs. However, the numbers are still lower than the energy and power which can be achieved by a combustion engine. Therefore, it is necessary to improve the performance of current EES devices further.

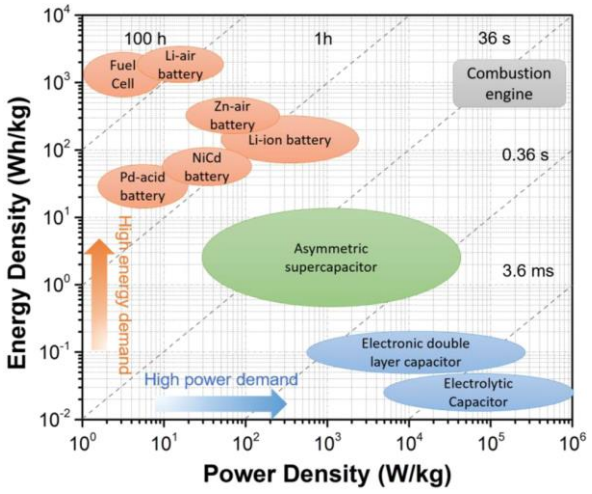

Figure 2.1. Ragone plot illustrating the performance in terms of specific power *vs* energy for different types of energy storage systems (mainly batteries and supercapacitors). (Ref.[11])

A typical dielectric capacitor is composed of two parallel conductive (*i.e.* metal) plates of area, *A*, that are separated by the distance, *d*. Within this, a non-conducting material (*i.e.* a dielectric material) such as paper, ceramic of dielectric constant *ε*, could be inserted between two metals (**Figure 2.2**). When the voltage, *V* is applied across the plates, charge, *Q* of equal magnitude and opposite polarization start to accumulate on the surface of the plates polarizing the dielectric material.

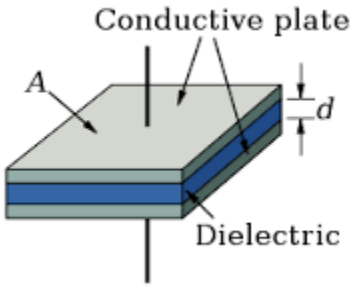

Figure 2.2. Dielectric capacitor (modified figure, web ref. [12])

The charge *Q* is proportional to the applied *V*, and the proportionality constant is known as the capacitance of the capacitor (since it denotes the ability of the capacitor to store charges). And it is expressed as follows;

$$C = \frac{Q}{V} \tag{2.1}$$

Where the charge *Q* is in coulombs (C) and voltage in volts (V). Hence, the capacitance is measured in C/V, *i.e.* Faraday, F.

Using Gauss's first law, electric field (E_{field}) is expressed as;

$$E_{field} = \frac{Q}{\varepsilon A} \tag{2.2}$$

By using electrodynamic relation of E_{field} and V, *i.e.*,

$$V = E_{field}\, d \tag{2.3}$$

Thus, by using equation 2.2 and 2.3 in equation 2.1, the capacitance can be expressed as,

$$C = \frac{\varepsilon A}{d} \tag{2.4}$$

Hence, the capacitance of a dielectric capacitor is directly proportional to the surface area of the conductive metal plates and inversely proportional to the distance between two plates. The permittivity of vacuum or free space, ε_o which is constant 8.854 x 10^{-12} $C^2/(N\ m^2)$ and ε_r is known as relative permittivity of the dielectric material defines the dielectric constant as $\varepsilon = \varepsilon_o \varepsilon_r$.

The energy density (E) and power density (P) of the capacitor can be formulated as follows[13];

$$E = \frac{1}{2} C V^2 \tag{2.5}$$

$$P = \frac{E}{t} \tag{2.6}$$

Where t, is the discharge time of the capacitor.

The electrochemical capacitors (also known as SCs), are composed of two electrodes where the charge-storage-active materials are deposited which are separated by a non-conductive porous membrane impregnated with a liquid or gel electrolyte. The electrodes are generally comprised of high surface area materials, such as porous carbons, activated carbons. Similar to a dielectric capacitor, SCs store charges through charge separation. However, in SCs, the charges are stored at the electrode-electrolyte interface. Hence, the interlayer distance between oppositely charged

layers is very small (in Å). Because of the effective surface area and smaller dielectric distance, SCs possess high energy and capacitance (1000 times higher) than dielectric capacitors[13] based on equation (2.4). Along with high energy and capacitance, the charge storage is highly reversible, SC can quickly charge-discharge and maintains low equivalent series resistance. Therefore, SCs have higher power density and longer lifetime than batteries.

2.2 Types of supercapacitors

SCs are characterized based on their working mechanism or based on the type of electrode material used for fabrication. Depending on the energy storage mechanism, SCs can be classified as;

(a) **Electric double-layer capacitors (EDLCs)** in which the energy is stored by adsorption of ions electrostatically across the electrode-electrolyte interface as shown in **figure 2.3 a.**

(b) **Pseudocapacitors (PCs)** whereby energy is stored due to the fast and reversible surface redox reactions, as shown in **figure 2.3.b.**

(c) **Hybrid supercapacitors (HSCs)** where the energy storage takes place by the combination of an electric double layer (EDL) formation and/or capacitive redox reactions at one electrode and non-capacitive (*i.e.* battery like) redox reactions on the other electrode, as shown in **figure 2.3 c**.[14]

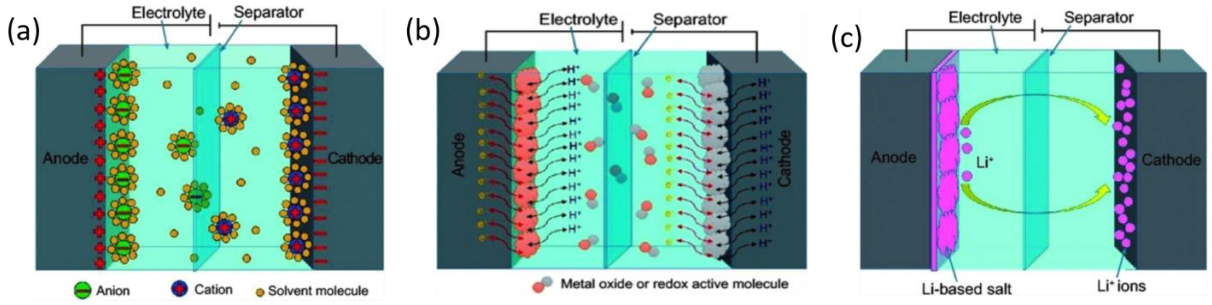

Figure 2.3 Schematics of Charge storage mechanism in (a) EDLCs (b) PCs (c) HSCs. (modified figure, ref.[14])

2.2.1 Electric double-layer capacitor (EDLC)

When two electrodes (composed of carbon) immersed parallel in the electrolyte solution, and voltage is applied across the electrodes, opposite charges are attracted at the electrode surface and form an ion layer on the surface separated by atomic distance (of few Å). This phenomenon is known as the formation of an electric double layer (EDL). Von Helmholtz first studied this effect, and the model is named as the Helmholtz model (**Figure 2.4a**).[15] Gouy and Chapman further studied the model; they considered the randomization of ions due to continuous thermal motion. Thus, they propose the Gouy and Chapman model, (**Figure 2.4b)**, where they describe the formation of diffuse layer of ions in electrolyte. However, this model predicts much higher EDL capacitance than the actual value.[14] Stern combined both Helmholtz and Gouy-Chapman models and introduced the Gouy-Chapman-Stern model (**Figure 2.4c**), that describe the formation of compact layer close to the surface of electrode as the Inner Helmholtz Plane (IHP) known as Stern layer and the diffused layer as the Outer Helmholtz Plane (OHP). Thus, the EDL capacitance can be obtained by combining the capacitance of a compact layer and diffused layer.[14]

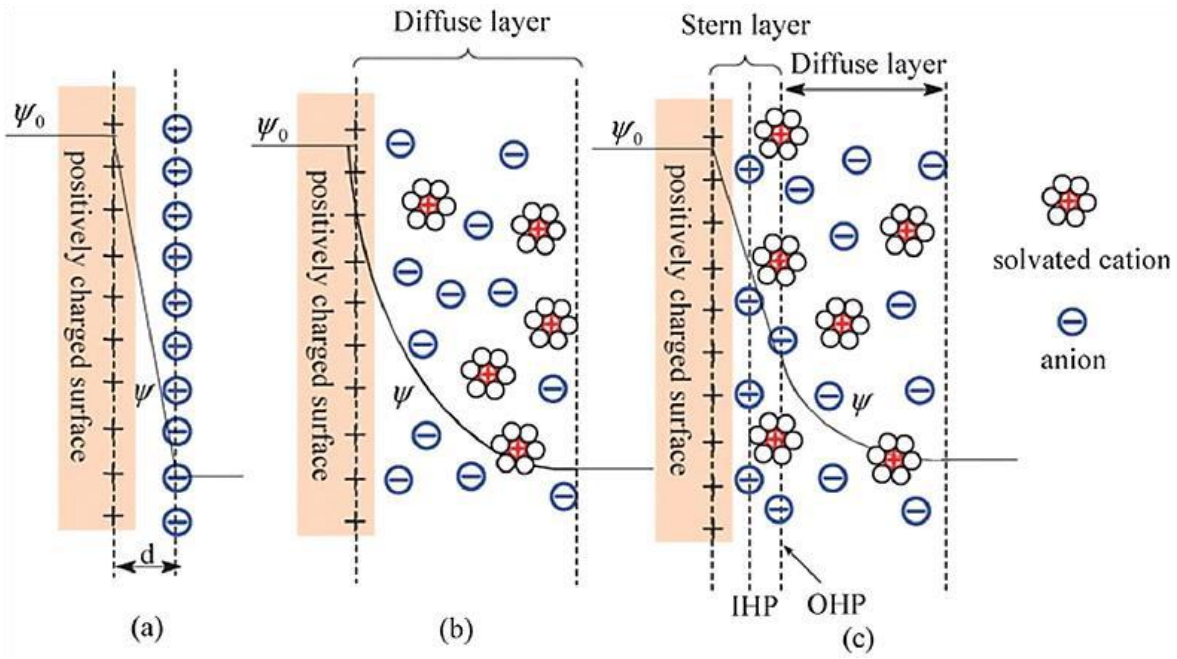

Figure 2.4 Schematic representations of electrical double layer charge storage mechanism explained by (a) the Helmholtz model, (b) the Gouy-Chapman model, and (c) the Gouy-Chapman-Stern model.(ref.[15])

Since there is no chemical conversion during the charge storage process, the EDLCs have excellent rate capability and long cycling stability. As well, large surface area of the electrode material can lead to high capacitance.[16] Moreover, they can provide high power density and thus fast charge-discharge because of the fast electrochemical processes. However, the energy density of EDLCs is an order of magnitude lower than the battery.[17] Various approaches are studied to enhance the surface area of the EDLCs, by using a different forms of carbons such as carbon nanotubes, graphene, activated carbon, porous carbon. However, sometimes in carbon derivatives (activated carbon, porous carbon) the high surface area does not enhance its electrochemical performance as expected because all pores (of different size) are not accessible to the electrolyte ions. Hence, the tuning of pore size to achieve significant electrode-electrolyte interaction is being developed,[18] and considered as one of the key parameters to enhance the performance of EDLCs. On the other

hand, the restacking of the graphene layers is a critical throwback that lowers the charge storage capacity of graphene based SCs.

2.2.2 Pseudocapacitors (PCs)

PCs are energy storage devices which exploit electrochemical mechanisms taking place in both EDLCs and batteries. PCs stores charges *via* a faradic process based on fast and reversible redox reaction on the surface or near-surface region of the electrode.[19] These faradic processes play a significant role on increasing the energy storage density of PCs compared to EDLCs. Unlike EDL capacitance, the pseudocapacitance arises due to charge transfer across the electrode-electrolyte interface (where charge rises linearly to applied potential) thus it is a non-electrostatic and faradic charge-storage process.[11,14] The pseudocapacitance can occur due to three different faradic mechanisms described by Conway and Gileadi[20] as depicted in **figure 2.5** namely;

(a) **Underpotential deposition;** in this process an adsorbed monolayer will form on the surface of electrode when potential is applied across the electrodes due to the reduction of different metal ions, resulting in a less negative potential than their equilibrium potential. Hence known as underpotential deposition (**Figure 2.5a**).[19] A typical example is a deposition of lead on the surface of gold.

(b) **Redox pseudocapacitance;** is the mechanism where adsorption of electroactive ions onto the surface or near-surface region of electrode materials takes place, and faradaic reactions occur with charge transfer (**Figure 2.5b**). Some transition metal oxides (such as RuO_2) and some conjugated polymers (Polyaniline), are examples of this mechanism.[19]

(c) **Intercalation pseudocapacitance;** this is the process, where the ions are intercalated-deintercalated rapidly in the bulk lattice of the electrode without changing the phase of the electrode material (for example, intercalation of Li-ion on Nb_2O_5) (**Figure 2.5c**).[19]

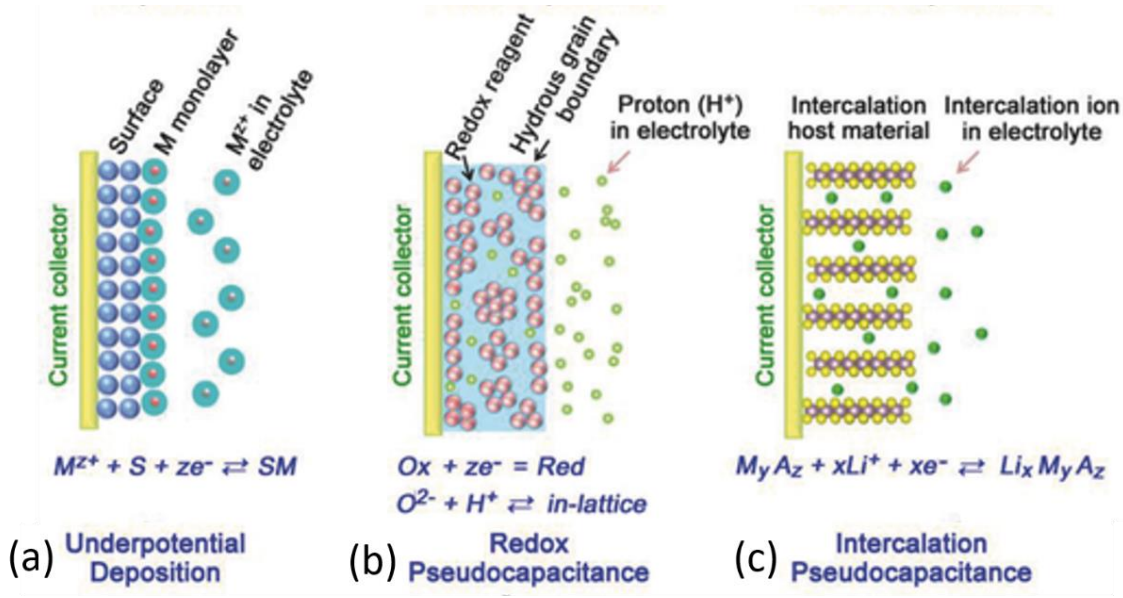

Figure 2.5 Schematic diagrams of the different faradaic processes that give rise to pseudocapacitance (modified figure, ref.[19]).

The pseudocapacitive materials can achieve high capacitance than EDL capacitive materials; nevertheless, the poor electric conductivity of PCs suppresses their cycling stability and lowers the power density.[14] Thus, often the pseudocapacitive materials are combined with conductive EDL capacitive material to enhance the stability.

2.2.3 Hybrid supercapacitors (HSCs)

To enhance the energy density of current supercapacitors their electrode materials and cell design are being studied and developed either by improving the material structure to enhance the specific capacitance or developing cell design that combines the electrodes of different charge storage

mechanism (*e.g.* one electrode of capacitive type and one electrode of battery type) to extend the cell voltage as a result it can improve energy of the device. Supercapacitors with such cell designs are categorized as HSCs.[21] In such SCs, battery-type electrode provides higher energy density than EDLC and capacitor type electrode provides higher power than batteries (*e.g.* Li-ion battery).[11,22]

2.2.4 Symmetric and asymmetric supercapacitors

Moreover, the SCs are classified as symmetric and asymmetric supercapacitors. When both electrodes of SCs store charges based on same storage mechanism (*i.e.* EDL formation and/or surface redox reactions) they are termed as **symmetric supercapacitors**. The full cells of F-N-co-doped carbon//F-N-co-doped carbon[23], MoO_3//MoO_3[24] are examples of symmetric capacitors. The SCs that are composed of two different active martials (that show same or different charge storage mechanism than each other) are known as **asymmetric supercapacitors**.[25] For instance AC// MnO_2[26], MnO_2/GO// Porous carbon[27] are examples of asymmetric supercapacitors. Further, symmetric and asymmetric supercapacitors can be differentiated, as depicted in **figure 2.6.**

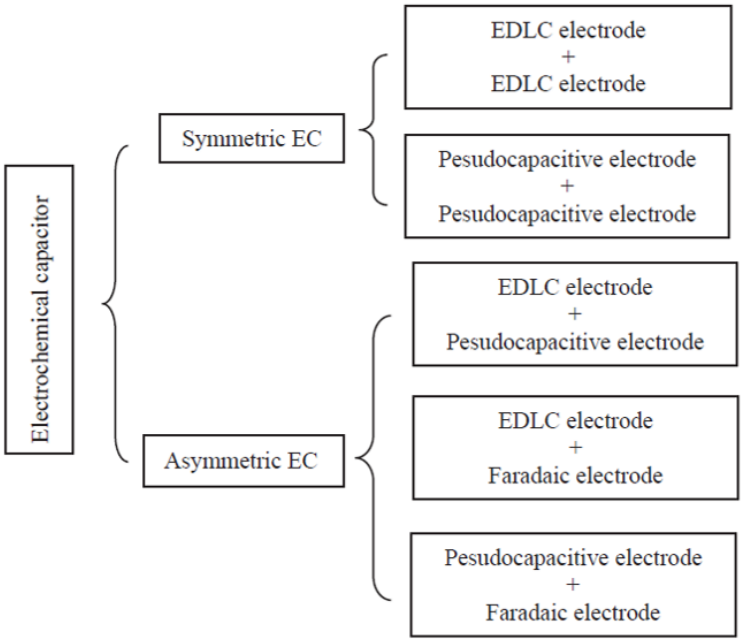

Figure 2.6. Classification of symmetric and asymmetric SCs.(adopted from ref.[25])

Due to different charge storage mechanisms on two electrodes HSCs are also considered as asymmetric supercapacitors. HSCs combine the advantages of capacitive charge storage mechanism and faradic mechanisms thus achieving high energy and power compared to other asymmetric and symmetric supercapacitors as depicted in **figure 2.7.**

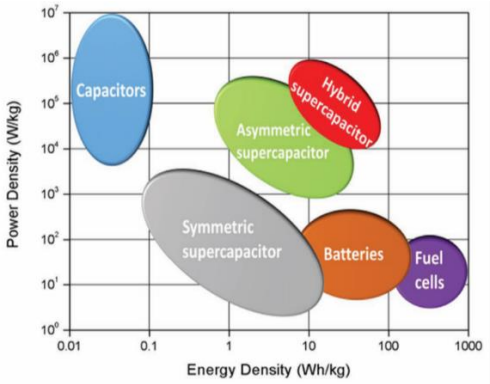

Figure 2.7. Ragone plot comparing energy and power densities of different types of SCs with batteries (modified figure[28]).

2.3 Electrochemical characterization

For symmetric devices the total capacitance is calculated as[29];

$$\frac{1}{C_{cell}} = \frac{1}{C_+} + \frac{1}{C_-} \tag{2.7}$$

Where, C_{cell} is the total capacitance of the cell, C_+ and $C_-$are the capacitance of at positive and negative electrode, respectively. However, in the symmetric device, both electrodes are prepared from the same material with an equal mass of active material, hence the capacitance of both electrodes are equal, $C_E = C_+ = C_-$. Moreover, the capacitance of the device is half of the capacitance of each electrode,

$$C_{cell} = \frac{C_E}{2} \tag{2.8}$$

For electrochemical characterizations of SCs materials, various techniques are developed, such as cyclic voltammetry (CV), galvanostatic charge/discharge (GCD) and electrochemical impedance spectroscopic (EIS) are widely used techniques to test the electrodes.

For asymmetric calculations; C_+ and C_- are made equal by using the charge balancing principle to balance the mass of active materials of both electrodes in such a way that $m_+ = \alpha\, m_-$.[11,29] Where α is the mass ratio ($0 < \alpha < 1$). That can be obtained as follows:

$$\frac{m_+}{m_-} = \frac{C_- V_-}{C_+ V_+} \tag{2.9}$$

where, V_+ and V_- are operating potential of positive and negative electrode respectively.

2.3.1 Cyclic voltammetry (CV)

The CV is a technique widely used for studying the electrochemical characteristics (such as operating potential, capacity, cyclic stability) and reaction mechanism (kinetics) of electrodes.[30] In the two/three-electrode system, voltage can be applied across the electrodes through a constant scan rate up to a certain voltage and it can be reversed to its initial voltage by applying opposite scan rate generating a cyclic voltammogram. The result is expressed as current versus potential or time. Here, the gradual change in voltage with time is known as scan rate, denoted as *v*, measured in mV/s.[29] The voltage is changed from initial (V_o) to maximum value (V_{max}) during a forward scan and then reversed to V_o during a backward scan. The voltage range from V_o to V_{max} is termed as operating voltage window (*V*). The instantaneous current (*i*) developed during the applied voltage upon varying scan rate is recorded, this current depends on the charge-storage process. Therefore, cyclic voltammogram instantly indicates the information about the operating voltage for the active material and the charge-storage mechanism. The electrodes consisting of purely EDL materials result in a rectangular shaped cyclic voltammogram, since EDL formation maintains steady current as the voltage increases further or decreases in operating voltage range. On the other hand, distorted cyclic voltammograms are the signature of redox reactions occurring on pseudocapacitive materials that consume slightly more time than EDL formation and thus the current change-rate varies when surface redox reactions take place.

The current dependence on scan rate can be expressed using the power-law relationship;

$$i\,(v) = av^b \tag{2.10}$$

where *a* is a constant and *b* is the power-law exponent.

The materials having capacitive charge-storage mechanism (whether it is rise due to EDL or pseudocapacitive reactions) indicate power-law exponent b = 1. Further, the materials showing strong redox peaks show b = 0.5 indicating the characteristics redox reactions of battery like electrode material.[31]

The total capacitance from cyclic voltammogram is calculated using **equation 2.1** as follows,

$$C = \frac{Q}{V} = \frac{S}{2v\,Vx} \tag{2.11}$$

Where S is the area under the voltammogram (that correspond to charge Q), v is scan rate, V is operating voltage, x can be mass, surface area, or volume of the electrode.

2.3.2 Galvanostatic charge/discharge (GCD)

The GCD is a widely used technique to obtain capacitance and to observe the stability of the SCs electrodes and cells. In GCD technique, a constant current is applied to the cell by limiting the voltage from V_o to V_{max}. The constant current flows through the cell until the voltage reaches from V_o to V_{max}, that is to charge or discharge the cell. The voltage *vs* time plot can be constructed to obtain the capacitance; it is also useful to estimate the internal resistance (IR drop). For the EDL capacitive materials, the voltage is linearly dependent on time while the current is constant, hence the charge-discharge profile shows triangular shape. Whereas for the pseudocapacitive materials charge-discharge profiles can deviate from linearity and the triangular shape. Further, specific capacitance based on the charge-discharge profile can be calculated as follows.

$$C_{sp.} = \frac{I\,\Delta t}{x\,\Delta V} \tag{2.12}$$

Where I is constant applied current, Δt is the discharge time, x stands for the mass (m), area (a), or volume (v) of an electrode or active material and $\Delta V = V_o - V_{max}$. Based on x the corresponding $C_{sp.}$ is termed as gravimetric capacitance (F g^{-1}), areal capacitance (F cm^{-2}), and volumetric capacitance (F cm^{-3}). For example, based on the mass, the specific capacitance can be calculated using **equation 2.12**.

$$C_{sp} = \frac{I\,\Delta t}{m_t\,\Delta V} \tag{2.13}$$

Where, m_t is the mass of active material on both electrodes,

2.3.3 Electrochemical impedance spectroscopic (EIS)

EIS is a spectroscopic technique that measures the impedance of the electrochemical cell (for example supercapacitor cell) as a function of frequency (generally ranging from 0.01 Hz to 100 kHz),by applying a low-amplitude alternating voltage (usually 5 mV) superimposed mostly on open-circuit voltage; however, any constant operating voltage could be used.[29] The obtained data are usually represented in Nyquist plot (**Figure 2.8**), and Bode plot (a plot of the log of amplitude of imaginary part of impedance (|z|) *vs* log frequency (*f*)) which shows the decrease in capacitance with increasing frequency and eventually becomes zero, *i.e.* it behaves like resistance. Hence, the capacitance can be calculated as,

$$C = \frac{1}{2\pi f |z|} \tag{2.14}$$

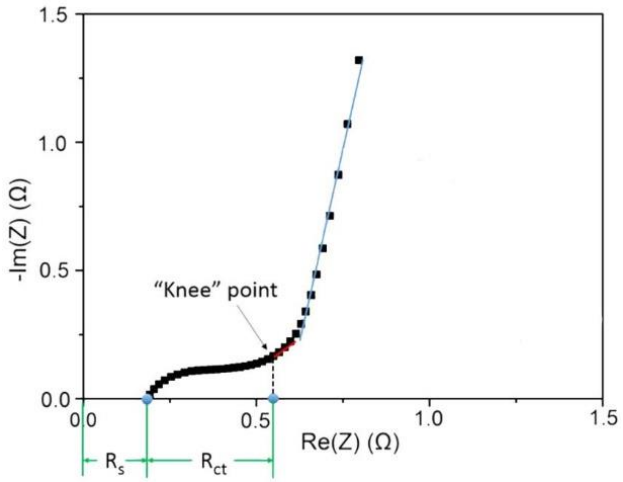

Figure 2.8 Nyquist plot recorded in a two-electrode system of a supercapacitor. (modified ref.[11])

The Nyquist plot is composed of three regions based on the information extracted by the frequency range. At the beginning of high frequencies (higher than 10^4 Hz), the Nyquist plot intersects the real axis denotes the electrochemical cell's internal resistance (**Figure 2.8**). Further, in the high to medium frequency region (10^4-1 Hz), it shows a semicircle followed by a beginning of the vertical line (with knee point) where the diameter of the semicircle represents the charge transfer resistance. At the low frequencies of less than 1 Hz, the plot shows a further vertical line referred to as pure capacitive ion diffusion, which should be parallel to the imaginary axis. However, due to the different diffusion rate at alternating current and redox process on an electrode surface, the plot deviates with an inclined angle lower than 90^o reflecting the combined contribution from the Warburg diffusion and ideal capacitive diffusion.[32]

2.4 2D materials and hybrids as supercapacitor electrode

Large surface area, good mechanical and chemical stability make 2D materials promising for supercapacitor electrodes.[33] Several 2D materials such as graphene, transition metal dichalcogenides (TMDs), black phosphorus, metal carbides/ nitrides (MXenes), metal

oxides/ hydroxides have been studied as supercapacitor electrodes.[34] These 2D materials can be further categorized in three different sub-classes based on the key property: (1) electrode materials with high-conductivity including semi-metallic and metallic TMDs, graphene and graphdiyne; (2) materials with high electrochemical-activity (such as pseudocapacitance), including MXenes, metal oxides and hydroxides, and layered double hydroxides (LDHs), and (3) materials with ultra-large-surface area, including metal-organic frameworks (MOFs), covalent organic frameworks (COFs),[34] and highly porous carbons.

Among these 2D materials, graphene is intensively studied for energy storage due to its good electric conductivity, high theoretical surface area up to 2675 m^2 $g^{-1,}$ and high theoretical capacitance (550 F g^{-1}).[35–37] Charge storage in graphene takes place through EDL formations. Despite this, so far, the capacitance obtained for graphene is lower than its theoretical capacitance. For example, fluffy layered and porous reduced graphene oxide film prepared by Xingke Ye *et al.* [38] achieved a capacitance of 238.4 F g^{-1} at the specific current of 0.5 A g^{-1}, maybe because of low surface area, 180.02 m^2 g^{-1}. The low surface area might be the result of the restacking of the layers, which reduces the active sites for adsorption and reduces the performance. The high performance can be achieved by enlarging the surface area, avoiding restacking, and making the surface accessible for the ions (*i.e.*, to have efficient ion diffusion).[35] Thus, the graphene can be modified *via* chemical functionalization and hybridization to improve its charge storage properties.

A key factor of energy storage devices is the energy density. For EDLC materials, energy density is lower than pseudocapacitor materials despite the stability and rate performance is better for EDLC. Thus, the effective strategy is to explore the hybrids prepared by combining the EDLC and pseudocapacitor materials with taking advantage of both properties. Therefore, intrinsic pseudocapacitive materials such as RuO_2 [39,40] and MnO_2 [41] were investigated extensively to

enhance supercapacitor energy. Along with these materials, researchers are also investigating Nb_2O_5 [21], FeO_x [42–44], CoO_x [45–47], NiO_x [48,49], and their sulfides [50,51]. Apart from their good electro-activity, the vast natural abundance, low cost, and environment-friendliness of iron oxides/hydroxides and sulfides render them as suitable candidates for sustainable energy storage devices.

CHAPTER 3
CHALLENGES AND OBJECTIVES

Challenges

Previous research efforts have demonstrated significant advancements in the exploitation of redox-active inorganic materials.[51–53] The analysis of these reports showed that the practical application of such systems could be improved if some solutions could be developed regarding matters related to the synthesis and operation of SC electrode materials, such as ;

(i) Developing cost-effective and facile synthetic routes (*i.e.*, one-pot and up-scalable), to firmly immobilize ultrasmall inorganic nanoparticles on the graphene matrix..[53]

(ii) Developing effective electrolytes that can provide high operating voltage windows and do not react with low-mass commercial current collectors such as Al foils. For instance, the aqueous electrolytes are corrosive (*i.e.*, they can oxidize the Al current collectors) and therefore require the use of high areal-mass and costly current collectors such as Ni foam[54], Fe[55], and Ti[56] foils, and as a result, these current collectors ultimately reduce the gravimetric performance of the device. Furthermore, the limited operating voltage window of aqueous electrolytes limits the device's energy content since it is proportional to the square of operating voltage.

(iii) The electrochemical performance of the electrodes should be optimized for high mass loadings (for practical application, mass loadings of ~10 mg are required[57]) to be applied in areas beyond thin film SC for small electronic circuit protection or power dissipation.

Objectives

The presented doctoral thesis aims to develop 2D composites of densely functionalized graphene derivatives (cyanographene, GCN) and ultrasmall nanoparticles of iron hydroxide and sulfides. By using simple, one-step, cost-effective, and up-scalable synthetic procedures, electrodes with increased electrochemical performance compared to the current state of the art were obtained. The purpose of the study was to:

(i) Develop seamless hybrids with good electronic and ionic conductivity through which the material can achieve good rate capabilities and cyclic stability.

(ii) Widen the operating voltage window (which enhances energy density) using non-aqueous electrolytes (*i.e.*, organic or ionic liquid).

(iii) Achieve paste-ready material that can allow the direct pasting on low areal-mass density current collectors.

(iv) Reduce the electrode's inactive mass to enhance overall device performance and make the material more suitable for practical use.

For this purpose, the seamless hybrid of GCN-iron oxyhydroxide (GCN-β-FeOOH further denoted as G(CN)ak) and GCN-greigite (GCNFe_3S_4) were prepared and studied as electrode materials for SCs. These materials significantly enhanced the energy of SC maintaining high power and excellent stability.

CHAPTER 4

EXPERIMENTAL PART

4.1 Synthesis of materials

4.1.1 Reagents and materials

Graphite fluoride, anhydrous iron chloride ($FeCl_3$), sodium cynaide (NaCN), poly (vinylidene fluoride) (PVDF), and N-methyl-2-pyrrolidone (NMP), thiourea, ethylene glycol (EG), Na_2SO_4, 1-ethyl-3-methylimidazolium tetrafluoroborate ($EMIMBF_4$), lithium bis(trifluoromethanesulfonyl)imide (LiTFSI) were purchased from Sigma-Aldrich. Acetone (pure), ethanol (absolute), urea, amine-free N, N-dimethylformamide (DMF), KOH were purchased from Penta. Carbon black was purchased from AkzoNobel (ketjen Black EC600, 1400 $m^2\ g^{-1}$). All reagents were used without further purification. Ultrapure water was obtained from Mirae ST instrument (Esse-UP Analysis, S00005812).

4.1.2 Synthesis of Cyanographene:

GCN was synthesized as previously reported[58] with minor modifications. Briefly, graphite fluoride (1 g) was dispersed in DMF (60 mL) in a round-bottom glass flask, kept for stirring for 1 day and then sonicated (Bandelin Sonorex, DT 255H type, frequency 35 kHz, power 640 W, effective power 160 W) for 4 h. Then, NaCN (2 g) was added and heated (130 $^{\circ}$C for 48 h under stirring at 600 rpm). The solution was allowed to cool down, and the solid was isolated and washed with centrifugation (in 15 mL vails) using DMF (2×), acetone (4×), ethanol (4×), and water (4×). In DMF and water, the solid was not properly precipitating. Thus we added 1% HCl (0.4 mL) in each vail, which facilitated total precipitation. After the last washing with water, the precipitate was

redispersed in water and kept for dialysis until the conductivity of the dispersion was below *c.a.* 150 μS cm^{-1}.

4.1.3. Synthesis of G(CN)ak hybrids:

We prepared the G(CN)ak hybrid by using a microwave-assisted synthesis method. Further, we obtained the hybrid with different content of β-FeOOH nanoparticles. In a typical synthesis of G(CN)ak-2, $FeCl_3$ (35 mg) and urea (63 mg) were dissolved into ultrapure water (1 mL) separately. In a microwave glass vial, GCN (30 mg) was dispersed in water (5mL), and the solutions of $FeCl_3$ and urea were added. The mixture was stirred (5 min.) and placed into the microwave reactor for 15min, at 100°C under stirring (600rpm). Then the mixture was purified by rinsing with water. G(CN)ak-1 and G(CN)ak-3 were produced by following the same procedure, except using 18 mg $FeCl_3$, 31 mg urea for G(CN)ak-1, and 69 mg $FeCl_3$, 125 mg urea for G(CN)ak-3. For comparison, GOak-2 was prepared using the same procedure as G(CN)ak-2 using GO instead of G-CN. GOak-2 was further reduced with hydrazine to produced GRak-2. The electrochemical performance was studied of these hybrids as a supercapacitor that is explained in section 5.1.2.

4.1.4 Synthesis of GCNFe_3S_4 hybrids:

The microwave-assisted synthesis method was used to prepare the hybrid with the Fe_3S_4 nanoparticles. In a typical synthesis of GCNFe_3S_4, $FeCl_3$ (53 mg) and thiourea (82 mg) were dissolved into ethylene glycol (1 mL) separately. In a microwave glass vial, GCN (45mg) was dispersed in EG (2mL), and the solutions of $FeCl_3$ and thiourea were added dropwise then 100 µl ultrapure water was added. The mixture was stirred (5 min.) and placed into the microwave reactor (microwave 300 Anthon par) for 5 min, at 180°C under stirring (600rpm). Then the mixture was purified by rinsing with ethanol. The electrochemical performance of this hybrid is studied as supercapacitor electrode that explained in section 5.2.2.

4.2 Characterizations

X-ray diffraction patterns (XRD) were recorded with a PANalytical X'Pert PRO MPD diffractometer in the Bragg-Brentano geometry, Co-K_α radiation (40 kV, 30 mA, λ = 0.1789 nm) equipped with an X'Celerator detector and programmable divergence and diffracted beam anti-scatter slits. The identification of crystalline phases was performed using the High Score Plus software (PANalytical) that includes the PDF-4+ database. Transmission electron microscopy (TEM; JEOL 2100) and Raman spectroscopy (Thermo Scientific, with a laser operating at a wavelength of 633 nm.) were performed to examine the structure of the materials. HRTEM images were obtained using an FEI TITAN 60–300 HRTEM microscope with an X-FEG type emission gun, operating at 300 kV. STEM–HAADF analyses for EDX mapping of elemental distributions on the G(CN)ak-2 sheets were performed with an FEI TITAN 60–300 HRTEM microscope operating at 80 kV. Thermogravimetric analysis (TGA; Netzsch STA 449C Jupiter thermal analyzer) under air (O_2) was performed to obtain the wt.% of β-FeOOH. The TGA instrument was equipped with a QMS 403 Aëolos mass spectrometer for evolved gases (EGA). The measurements in synthetic air (100 $cm^3 \cdot min^{-1}$) were carried out using an open crucible made of α-Al_2O_3, from 45 °C to 1000 °C and a heating rate of 10 $K \cdot min^{-1}$. The EGA was focused on m/z 18, 44, 48, and 64 for H_2O, CO_2, SO, and SO_2, respectively. XPS was carried out with a PHI VersaProbe II (Physical Electronics) spectrometer using an Al Kα source (15 kV, 50 W). The obtained data were evaluated with the MultiPak (Ulvac - PHI, Inc.) software package.

The ^{57}Fe Mössbauer spectra were measured employing a home-made Mössbauer spectrometer operating in the transmission geometry and constant acceleration mode and equipped with a 50 mCi ^{57}Co(Rh) radioactive source. For low-temperature measurements, the sample was placed

inside the chamber of the cryostat (Oxford Instruments, UK), to which the Mössbauer spectrometer is connected. The isomer shift values were referred to metallic α-Fe at room temperature.

4.3 Electrode preparation and electrochemical characterizations

A three-electrode open cell configuration was used for the preliminary electrochemical testing of the hybrids. The 1 M Na_2SO_4 aqueous solution was used as the electrolyte, a platinum electrode as the counter electrode and Ag/AgCl as the reference electrode. The samples were deposited on a glassy carbon electrode (GCE), as follows: sample suspension (10 μl, 2mg mL^{-1}) was drop-coated on GCE and allowed to dry in the air at room temperature.

For the preparation of full cell, the active material, carbon black and binder PVDF in the weight ratio 90:5:5 were dispersed into NMP to prepare a homogenous slurry. The slurry was prepared using planetary vacuum mixer. Using doctor blade this slurry was deposited on Ni foam (purchased from MTI; EQ-bcnf-80um) and on Au electrode for testing it into the aqueous electrolyte, and on carbon-coated Al foil (purchased from MTI; EQ-CC-Al-18u-260) for testing in organic and ionic liquids ($EMIMBF_4$ + LiTFSI). The G(CN)ak-2 is tested as a redox-active negative electrode in KOH electrolyte, porous carbon (ACS Material, LLC, product number: CNP00001, surface area of 2000 m^2 g^{-1}) was used as the positive electrode in an asymmetric full cell. The pasted electrodes were then dried into a preheated furnace at 120 ºC for 2 h and further transferred into vacuum drier where electrodes were heated overnight at 60 $^{\circ}$C or 70 $^{\circ}$C. Following, the cell was assembled using PAT-cell testing system (purchased from EL-CELL GmbH, Germany) and tested with Biologic instrument (BCS-810) equipped by BT-lab software. Electrochemical impedance spectra were also obtained using the full cell devices in the frequency range from 0.01 to 100 kHz with an AC amplitude of 10 mV.

Specific capacitance, energy density, and power density were calculated by the equations below,

$$C = \frac{I}{m}\frac{\Delta t}{\Delta V}\ in\ F\ g^{-1}, \tag{4.1}$$

$$E = \frac{1}{2}\frac{CV^2}{3.6}\ in\ Wh\ kg^{-1}, \tag{4.2}$$

$$P = \frac{3.6\,E}{\Delta t}\ in\ kW\ kg^{-1} \tag{4.3}$$

where, I, is the applied current, Δt is time in seconds required for discharge, ΔV is operating potential/voltage, m is the total mass of both electrodes (including graphene and inorganic phases, as well as carbon black, polymeric binders and current collectors). In cases where the mass of the current collectors is not included, it is stated in the text.

The performance was also calculated by using integral equations for non-linear galvanostatic charge-discharge curves, for the sake of more accurate metrics, which are available in **table B2, appendix B.**

$$E = \frac{I}{m}\frac{\int V dt}{3.6}\ \text{in}\ F\ g^{-1} \tag{4.4}$$

where V is the operating voltage, and I/m is the specific current, where m is the mass in both electrodes.

CHAPTER 5

RESULTS AND DISCUSSION

5.1 Densely functionalized cyanographene bypasses aqueous-electrolytes and synthetic limitations toward seamless graphene/β-FeOOH hybrids for supercapacitors:

5.1.1 Synthesis and material characterization.

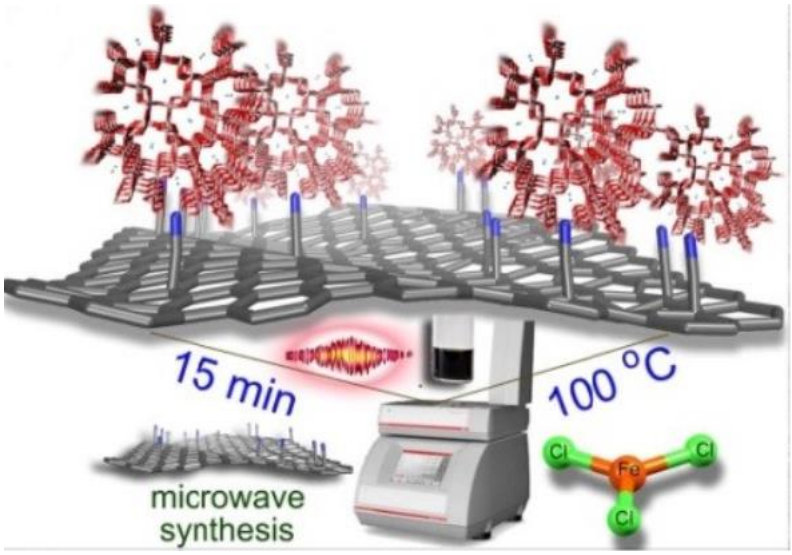

Figure5.1: Schematic representation of the synthesis of G(CN)-ak hybrid.

The graphene derivative, cyanographene (GCN), because of its high conductivity (500 S m^{-1}) and a very high degree of functionalization (*i.e.,* around 12-15%), was selected as the conductive support for the hybrid. Moreover, the β-FeOOH can strongly bind to GCN through the nitrile groups to avoid aggregation of β-FeOOH nanoparticles and to prevent the restacking of graphene nanosheets. Therefore, first, the GCN was prepared from fluorographite, as reported previously.[58] Afterwards, the seamless GCN/ β-FeOOH hybrid named G(CN)-ak was synthesized using a simple, one-step, and fast microwave-assisted synthesis method. In a typical synthesis, the dispersion of GCN, $FeCl_3$, and urea in ultrapure water was mixed and microwaved for 100°C for 15 min **(Figure 5.1)**. Further, the hybrids with increasing content of β-FeOOH were synthesized

to study the optimum concentration of β-FeOOH in hybrid to achieve effective electrochemical performance. The hybrids obtained with different concentration denotes as G(CN)ak-1, G(CN)ak-2, and G(CN)ak-3.

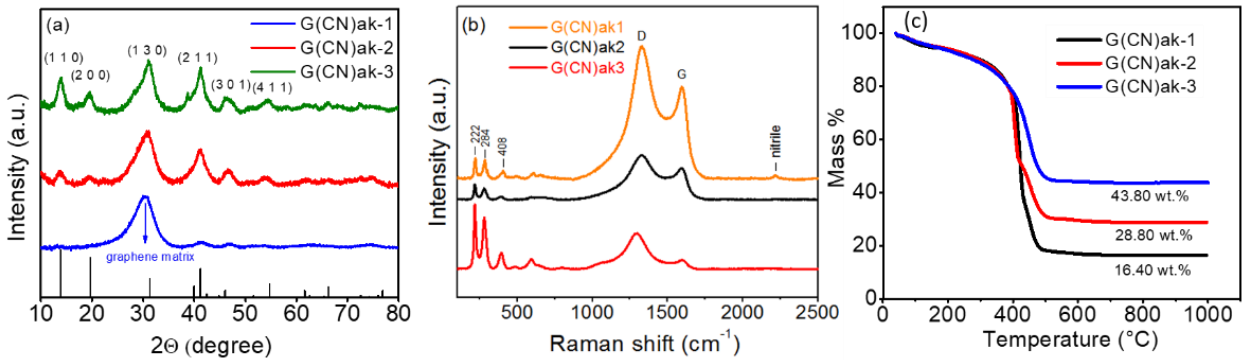

Figure 5.2. (a) XRD pattern (ICDD card number 01-075-1594 for *β*-FeOOH appears as bars) and (b) Raman spectra of G(CN)ak-1, G(CN)ak-2 and G(CN)ak-3 hybrids. (c) TGA curves under air of the G(CN)ak-1, G(CN)ak-2, and G(CN)ak-3 hybrids to determine the approximate inorganic content in the hybrids. (modified figure from ref.[59])

The β-FeOOH phase formation was confirmed in the hybrids using X-ray diffraction and Raman spectroscopy. **Figure 5.2a** shows the XRD patterns of the three G(CN)-ak hybrids. The characteristic diffraction peaks for β-FeOOH are visible in the diffraction patterns of the hybrid. The spectra show a high intense diffraction peak at 30 degrees because of the contribution of the graphene matrix. Raman spectra of hybrids showed the characteristics peaks of the β-FeOOH phase and graphene matrix, as indicated in **figure 5.2b** hence confirm the presence of the FeOOH with graphene matrix.

Further, the inorganic content was identified using thermogravimetric analysis, and the content observed in G(CN)ak-1 is ~16 wt%, G(CN)ak-2 is ~29 wt%, and in G(CN)ak-3 is ~ 44 wt% (**Figure 5.2c**). However, it should be noted that while heating hybrid under air the FeOOH is

transformed into hematite. The observed content is useful for the direct comparison of hybrids only.

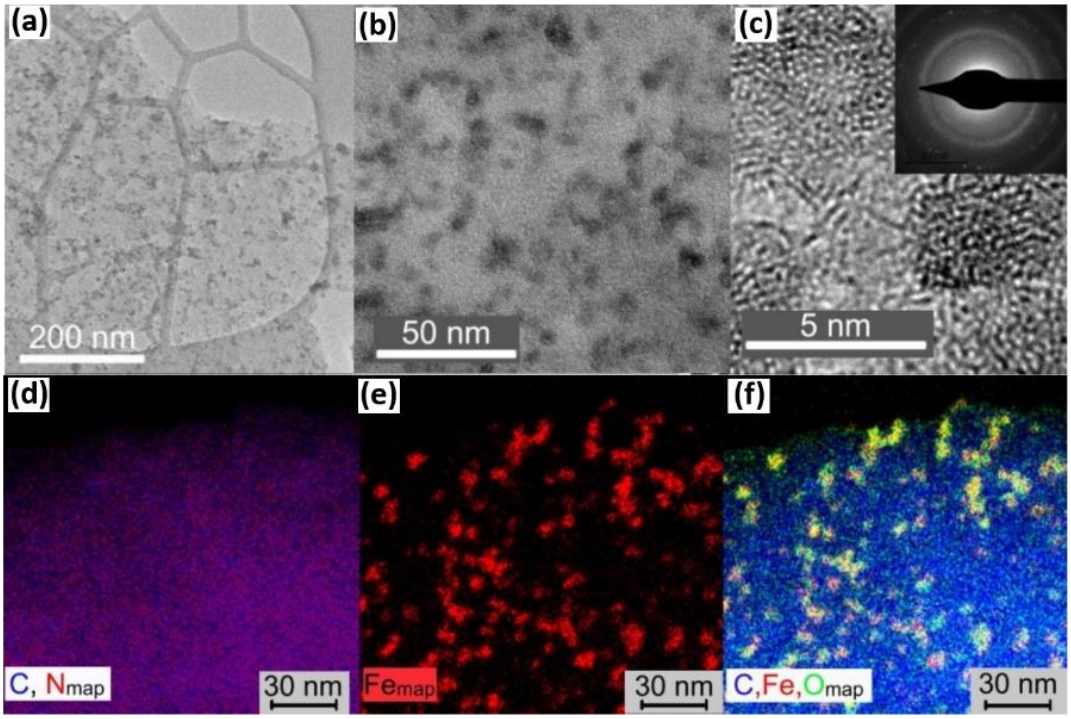

Figure 5.3. (a-c) Transmission electron micrographs of the G(CN)ak-2 hybrid, with SAED pattern in the inset of panel (c) and (d-f) corresponding elemental mapping for (d) carbon and nitrogen, (e) iron, and (f) carbon, iron and, oxygen.

The morphology of the prepared hybrid was observed using high-resolution transmission electron microscopy (HR-TEM). The HR-TEM showed the uniform and homogeneous distribution of β-FeOOH nanoparticles on GCN nanosheets (**Figure 5.3a, b**). The ultra-small β-FeOOH nanoparticles with a mean size distribution of *c.a.* 3 nm were unable to show well-defined crystal planes (**Figure 5.3c**) and clear diffraction points, as shown in selected area diffraction (SAED) pattern (**Figure 5.3c, inset**). The effective surface area and highly accessible active sites improve the rate-capability of an electrochemical cell. Thus, nanosizing and nano-confinement enhance rate performance.[22,60–62] The EDXS elemental mapping showed the dense distribution of N from nitrile

group on graphene sheet showing the high functionalization of GCN (**Figure 5.3d**) and uniform distribution of Fe and O elements on GCN is confirmed (**Figure 5.3e, f**). Further, the co-existence of Fe and O (**Figure 5.3f**) confirmed the Fe_xO nature of the nanoparticles.

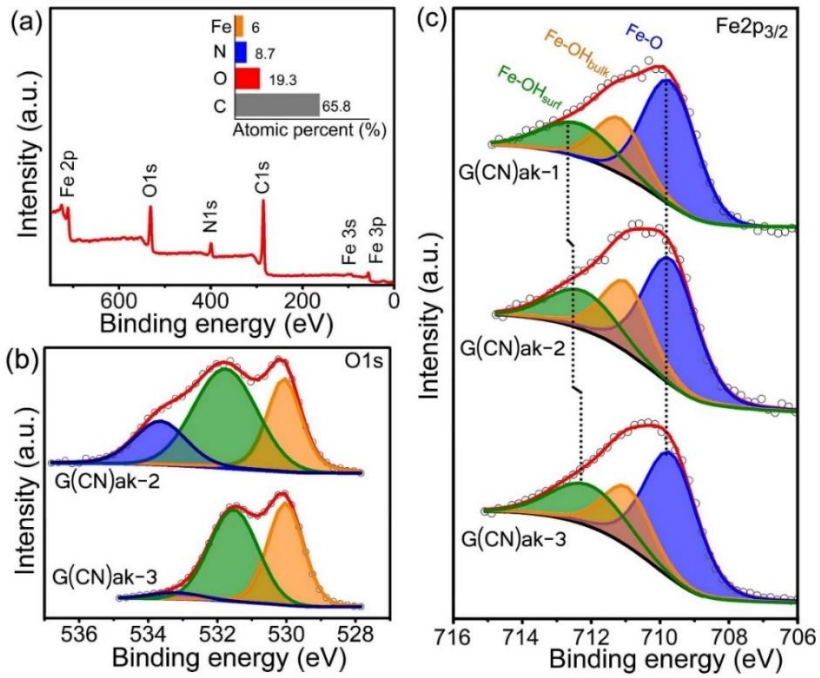

Figure 5.4. (a) X-ray photoelectron emission survey and elemental analysis (inset) of the G(CN)ak-2 hybrid. Deconvoluted X-ray photoelectron emission spectra for the (b) oxygen region of hybrid G(CN)ak-2 and -3, and (c) iron region of all three G(CN)ak hybrids. (modified figure, ref.[59])

The high-resolution X-ray photoelectron (HR-XPS) was employed to confirm the elements present in the hybrid. Fe, C, O, and N were identified the N were present in high content, which verified the high functionalization of graphene with nitrile groups (**Figure 5.4a**). The hybrid G(CN)ak-2 showed a new binding energy component at 533.6 eV. This energy should be ascribed to the surface OH groups interacting strongly with GCN.[43,63,64] Other than 533.6 eV, the two typical components of β-FeOOH at 530 eV (Fe-O-Fe) and 531.7 eV(Fe-O-H) has observed for both G(CN)ak-2 and G(CN)ak-3(**Figure 5.4b**).[65,66] "The interaction of OH group is also confirmed by

the deconvolution of the Fe $2p_{3/2}$ envelope with three components according to the crystal structure of β-FeOOH (*i.e.*, Fe-O, Fe-OH_{bulk}, and Fe-OH_{surf}, **Figure 5.4c**); the Fe-OH species are positioned both on the outer facets of the crystal (Fe-OH_{surf}), and on the bulk (Fe-OH_{bulk}), towards the inner pores.[67]" However, the interaction between surface -OH group and the GCN increases as the β-FeOOH content has become lower in hybrid. Further, this strong interaction has supported by Mossbauer spectroscopy.

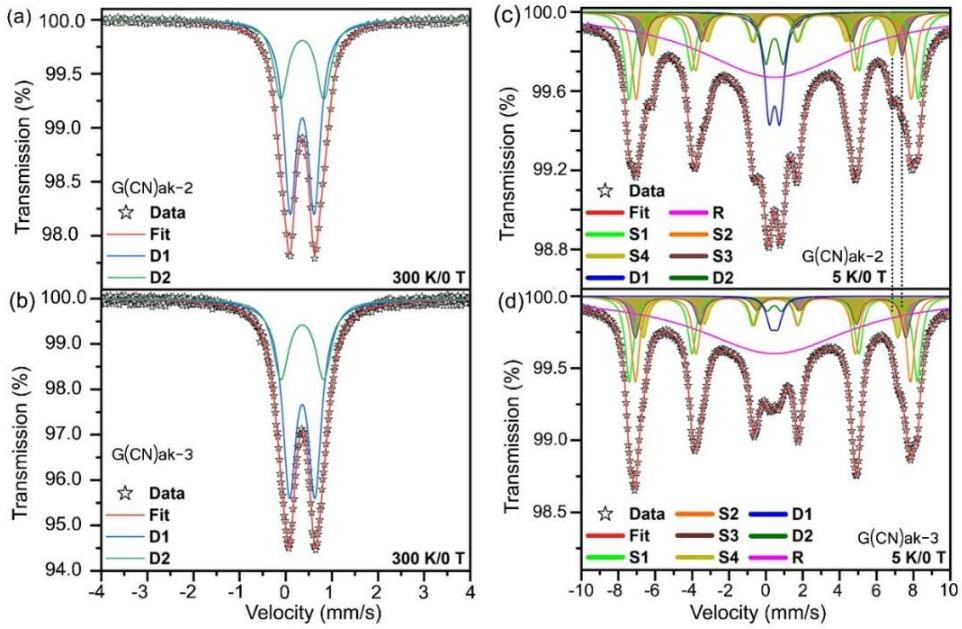

Figure 5.4. [57]Fe Mössbauer spectra of G(CN)ak-2 and G(CN)ak-3, respectively, were recorded without an external magnetic field. Deconvoluted Mössbauer spectra at a temperature of 300 K (a) for G(CN)ak-2 and (b) for G(CN)ak-3. Deconvoluted Mössbauer spectra at temperature 5 K (c) for G(CN)ak-2 and (b) for G(CN)ak-3. The S3 and S4 deconvoluted sextets filled with solid colour (in panel c, d) represent the Fe coordination sites which appear to be affected by the G-CN matrix in the G(CN)ak-2 hybrid. (modified figure, ref.[59])

For detailed analysis, [57]Fe Mossbauer spectra have recorded for G(CN)ak-2 and -3 samples at temperature 5 K and 300 K. More specifically, at temperature 300 K, the non-Lorentzian profile

of the ^{57}Fe Mössbauer spectrum of both samples was correctly fitting, assuming a mathematical model with two doublet components (see **Figure 5.4a, b and, appendix table A1**). The observed spectra do not show magnetic splitting evidencing that the iron-containing nanoparticles are in the superparamagnetic state. The analysis provided the values of isomer shift (δ) and quadrupole splitting (ΔE_Q) of the two doublets (see **appendix table A1**), which are in the interval of β-FeOOH. Further, the absence of additional components confirmed the presence of pure β-FeOOH in both samples.

The ^{57}Fe Mossbauer spectra recorded at 5 K showed dramatic change (**Figure 5.4 c, d**) for both samples. The spectra fit with four sextets (correspond to the magnetically split pattern), two doublets (correspond to relaxing components), and one singlet. This corroborates to a commonly accepted scenario of the coexistence of superparamagnetism and magnetically blocked states due to a particle size distribution.[68] The quadrupole splitting (ΔE_Q) values for sample G(CN)ak-3 were identical to those previously reported for β-FeOOH nanoparticles. Compare to these values, G(CN)ak-2 showed lower values. "A variation in the ΔE_Q parameter reflects changes in the distribution of the electric ligand field around the probed iron atom; it tends to zero for the spherically symmetric electric environment. Thus, for G(CN)ak-2, reduction in ΔE_Q-value of S3 and S4 components could be interpreted in terms of changes in distribution. Moreover, the orientation of the ligand field acting on the Fe_1 and Fe_2 sites close to chloride vacancy. In other words, this implied that these sites were involved in the interaction with the surrounding G-CN matrix, as evidenced by XPS analysis."

5.1.2 Electrochemical characterizations

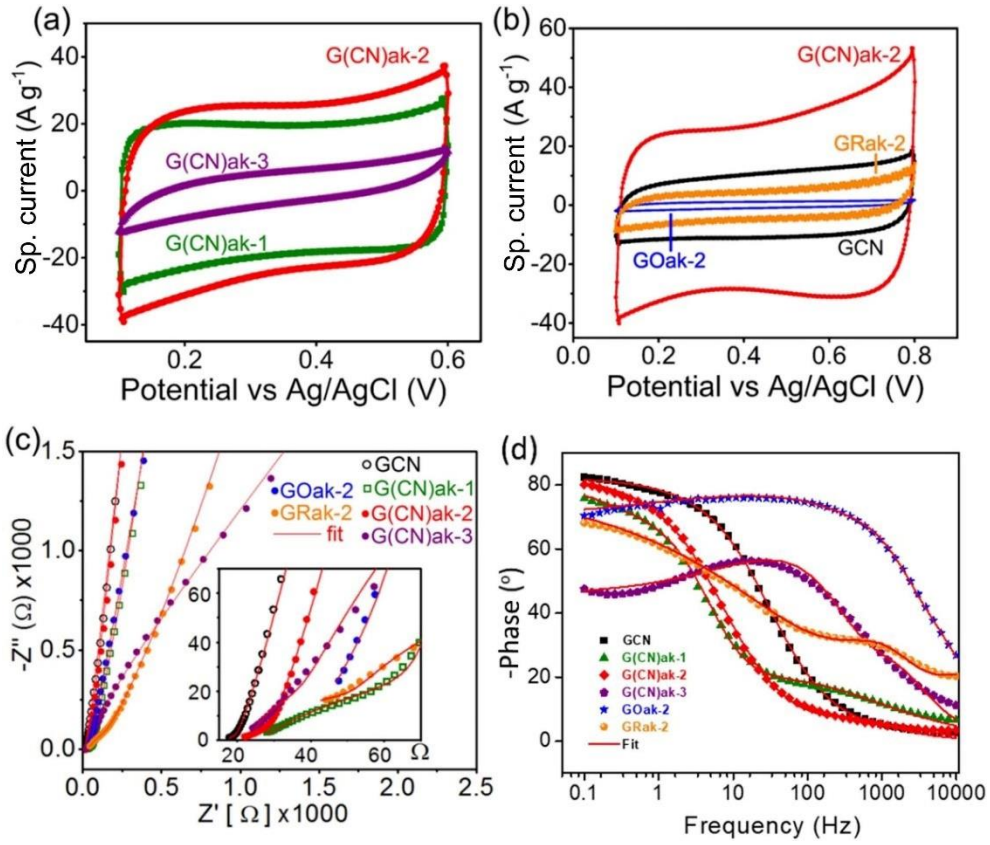

Figure 5.6. (a) Cyclic voltammograms of the hybrids with increasing *β*-FeOOH content (G(CN)ak-1, -2 and -3), (b) Cyclic voltammograms of the G-CN, G(CN)ak-2, GOak-2 and GRak-2 recorded at scan rate 100 mV s^{-1}. For GCN, the all three G(CN)ak hybrids, GOak-2 and GRak-2, (c) Electrochemical impedance spectra, the inset is focused on the beginning of the axis at the high-frequency region and, (d) Bode plots. (modified figure[59])

The optimum mass of *β*-FeOOH in the hybrid was determined by investigating the performance of the G(CN)ak hybrids prepared with different conc. of iron in a three-electrode cell using cyclic voltammogram. Where cyclic voltammogram indicated that the G(CN)ak-2 had the desired mass

ratio since it had the highest area under the *i*/E curve (**Figure 5.6a**) because the area is proportional to the capacitance of the material.

Moreover, the cyclic voltammogram obtained for pure GCN indicated the critical role of *β*-FeOOH to enhance the performance of the hybrid (**Figure 5.6b**). Further, the cyclic voltammogram of G(CN)ak-2 has compared with the hybrid obtained using graphene oxide (GO) as the conductive matrix for *β*-FeOOH nanoparticles denoted as GOak-2 prepared by the same synthetic method and further reducing it with hydrazine to obtain graphene/*β*-FeOOH (GRak-2). However, these hybrids showed low specific current, and smaller areas under cyclic voltammograms compare to G(CN)ak-2. Electrochemical impedance spectroscopy (EIS) has performed to study the effect of the presence of *β*-FeOOH nanoparticles embedded on GCN. The Nyquist plots obtained for all hybrids and pure GCN showed the internal resistance of G(CN)ak-2 electrode (at high frequencies, the intersection of a plot to the real axis) is much lower than other hybrids (inset **figure 5.6c**). As well its slope of the inclined line is almost equal to the pure GCN that indicate good ion diffusion in G(CN)ak-2 (**Figure 5.6c**),[69] also G(CN)ak-2 showed the higher phase angle of 81° almost same as the pure GCN (82°) (**Figure 5.6d**). However, as the iron content was increased, the diffusion rate was lowered (evidenced from lower slope of the inclined line, **Figure 5.6c**). And the phase angle is lowered up to 48°, suggest unavailability of the active site on the electrode surface, which was supported by the TEM images of hybrid G(CN)ak-3 that showed the densely covered GCN with *β*-FeOOH NPs (**appendix A, figure A1b**).

Further to study the charge storage properties of G(CN)ak-2 in the real device, the symmetric full-cell was tested in aqueous 1 M Na_2SO_4 (**Figure 5.7a**). The galvanostatic charge-discharge curves obtained at the low specific current (*i.e.* at 2.5 A g^{-1}) where the diffuse layer is thick because

more time is available for the possible surface adsorption and redox reaction to take place, the galvanostatic charge-discharge curves are slightly distorted from their triangular shape indicating minor pseudo-capacitance contribution. The full cell achieved energy around 6.1 Wh kg^{-1} at power 8.5 kW kg^{-1} for specific current 10 A g^{-1} (**See appendix A, table A3**). In addition, the energy and power were calculated using high mass Ni foam as a current collector, the values are further lowed to energy 0.3 Wh kg^{-1} at power 0.4 kW kg^{-1} which is much lower than previous reports presented in **appendix A, table A2.** For example, α-Fe_2O_3 nanoparticles embedded on graphene[70] delivered energy around 4.2 Wh kg^{-1} and power of 1.4 kW kg^{-1}, with respect to the total mass, Another example is of Fe oxide nanoparticles combined with graphene[71] delivered high energy and power of 4.0 Wh kg^{-1} at 3.9 kW kg^{-1}.

However, several reports listed in **appendix A, table A2** used costly and high mass current collectors such as Ti foil,[72] carbon cloth,[70,71] nickel foam[71,52], to achieve seamless interaction among electrode and active material. Further, the use of aqueous electrolyte limits the voltage window hence the energy density. On the other hand, the use of organic electrolyte permits the use of cost-effective, low mass current collectors (*i.e.* commercially used Al foils) and increase the operating voltage window. Further, the good wettability in an organic electrolyte and effective ion diffusion through the electrode material enhances the electrode performance.[73] Therefore, wettability/ solvation of G(CN)ak-2 hybrid were tested and compared with hybrids GOak-2 and GRak-2, which has prepared under identical conditions. In general, the hybrids were mixed with $LiPF_6$ in PC (organic electrolyte) and placed aside without any movement and observed with time.

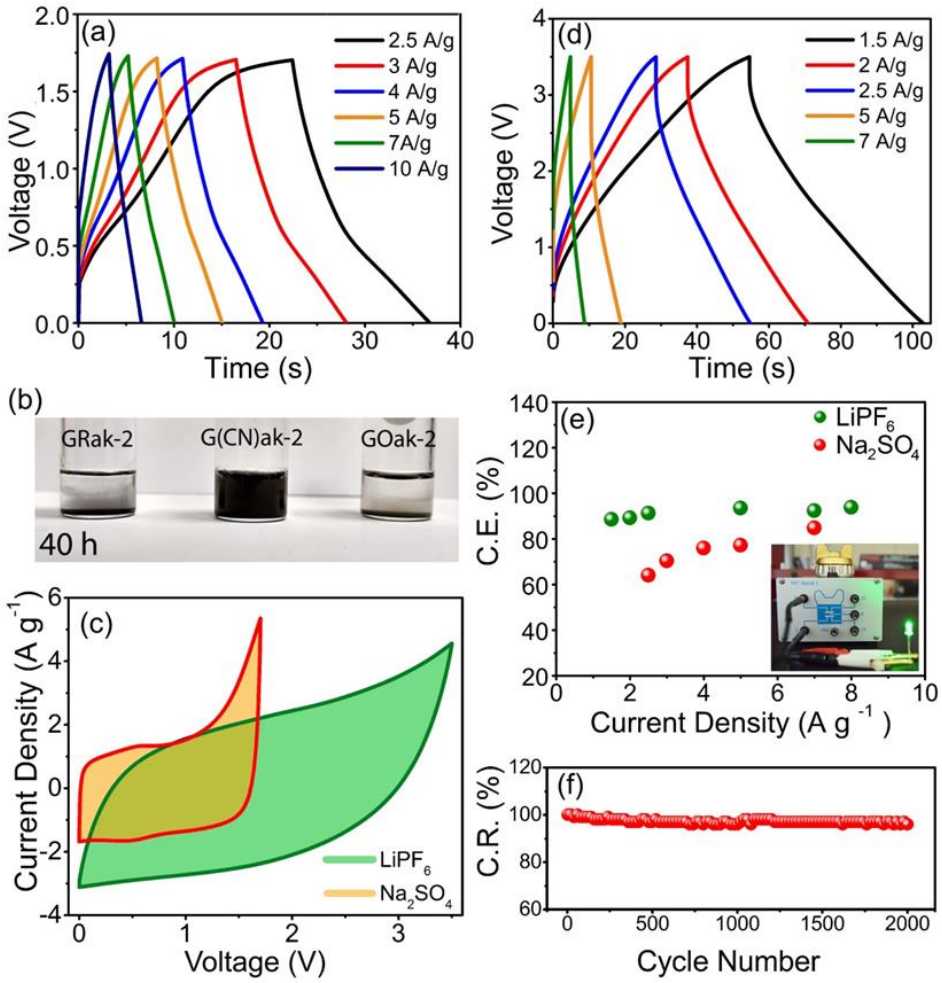

Figure 5.7. Electrochemical response of the G(CN)ak-2 symmetric device in (a) 1M Na_2SO_4 as recorded with galvanostatic cycling at increasing specific current. (b) wettability/stability of hybrids prepared from reduced GO and *β*-FeOOH (GRak-2), G(CN)ak-2 and GO with *β*-FeOOH (GOak-2). (c) Cyclic voltammograms at scan rate 100 mV s^{-1} in aqueous and organic electrolyte. (d) Galvanostatic charge-discharge curves in propylene carbonate with 1 M $LiPF_6$ at increasing specific current. (e) Coulombic efficiency (C.E. %) in the two different electrolytes at increasing specific current. Inset: a charged electrochemical cell inside its testing station connected directly to a green LED and (f) capacity retention (C.R.%) upon cycling. (ref.[59])

After 40h only hybrid G(CN)ak-2 have not shown precipitation (**Figure 5.7b**) indicating good solvation and stabilization compare to GOak-2 and GRak-2. "Although graphene has affinity for organic electrolytes, sheet restacking, aggregation and lack of polar groups for interaction with ions is a significant hurdle, stimulating significant research.[73]" Hence a full cell of G(CN)ak-2 were further evaluated using organic electrolyte, which extended the operating voltage window from 1.7 V (in aqueous electrolyte) to 3.5 V (**Figure 5.7c,d**). Due to the good solvation in organic electrolytes the coulombic efficiency (CE) of full cell is also increased (**Figure 5.7e**) to 93% where in aqueous electrolyte it was 68 % at specific current 2.5 A g^{-1}. As a result, the performance is improved that reflects in terms of significantly increased energy up to 20 Wh kg^{-1} at power 8.7 kW kg^{-1} considering active mass (**Table S4**). In addition, the performance based on the total electrode mass is increased more than 10-fold (5.2 Wh kg^{-1} at 5 kW kg^{-1}) compared to performance in aqueous electrolyte.

The obtained gravimetric results were further compared with the current state of the art with normalizing the reports to standard metrics (see **appendix A, table A2**), the comparison was summarized in the plot in **Figure 5.8**. Where the only point 36 showed the high performance though, it's multistep and complicated synthetic procedure makes it incompatible for practical application.[52] " It should be emphasized, that taking advantage of the high ionic transport of the hybrid, as previously discussed, commercially relevant electrode mass loadings were effectively used (see **appendix A, table A2** for details), which is an essential prerequisite for building SC with true application potential.[41,57,74]"

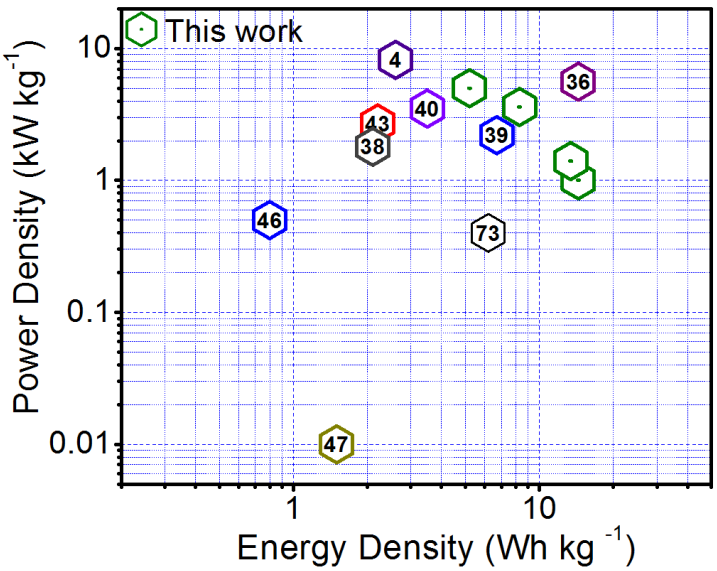

Figure 5.8. Comparing the energy and power of the G(CN)ak-2 hybrid with state-of-the-art reported materials based on metal oxides and mostly iron oxides. All values were normalized as described in detail in **appendix A, table A2** and calculated including the mass of the current collectors (full details are available in **table A2**). The numbers shown in the plot correspond to the respective reports, in which the following anode//cathode materials were used: **[4]** Fe_2O_3/FGS//MnO_2/FGS,[72] **[36]** FeOOH // $NiMoO_4$,[52] **[38]** $CuCo_2O_4$ / CuO // RGO/ Fe_2O_3,[75] **[39]** Fe_2O_3-QDs–3D GF // 3D HPG ,[70] **[40]** Porous Mn_3O_4// Fe_3O_4,[71] **[43]** Fe_3O_4@ Fe_2O_3 // Fe_3O_4@ MnO_2,[56] **[46]** FeOOH // Co–Ni double hydroxides,[48] **[47]** NiO NSAs@ Co_3O_4-NiO FTNs // AC@NF,[76] **[73]** Fe_3O_2@rGO // carbonized PANI nanorods[77]. (ref.[59])

Along with this enhanced gravimetric performance, the seamless hybrid has achieved high areal energy of 126.6 µWh cm^{-2} at power 55.5 mW cm^{-2} and improved volumetric energy and power up to 5.3 mWh cm^{-3} at 2.3 W cm^{-3} at high mass loading of around 14 mg. Thus, the G(CN)ak-2 hybrid proved itself as a promising electrode material for supercapacitor. However, further improvements are anticipated to growing hybrids that can be used as a cathode for asymmetric SCs or even as battery electrodes.

5.2 Pinning ultrasmall greigite nanoparticles on graphene for effective transition-metal-sulfide supercapacitors in an ionic liquid electrolyte:

5.2.1 Synthesis and material characterization.

The ultrasmall nanoparticles of greigite were immobilized on highly conductive cyanographene using simple one-step, and rapid microwave-assisted synthesis method. In the typical synthesis of GCNFe_3S_4 hybrid, GCN dispersed in ethylene glycol and $FeCl_3$, thiourea was dissolved in ethylene glycol separately. Further, by mixing all solution, they were treated in the microwave reactor for very few mins. (5 min.) at temperature 180 $^{\circ}$C later the paste ready hybrid was extracted. Moreover, we prepared pure greigite following the same procedure in the absence of GCN. In the hybrid, nitrile functional groups firmly bind the greigite nanoparticles to the GCN support and confine the size of nanoparticles (less than 5 nm diameter, **Figure 5.2.1a**) preventing aggregation of nanoparticles and restacking of graphene nanosheets. Whereas, in the synthesis of bare greigite absence of GCN lead into the formation of large particles (*ca.* 40 nm, **appendix B, Figure B1c**) highlighting the key role of GCN in hybrid. This size confinement is crucial for providing a large number of active sites available for interaction and for allowing fast surface redox process.[31,78]

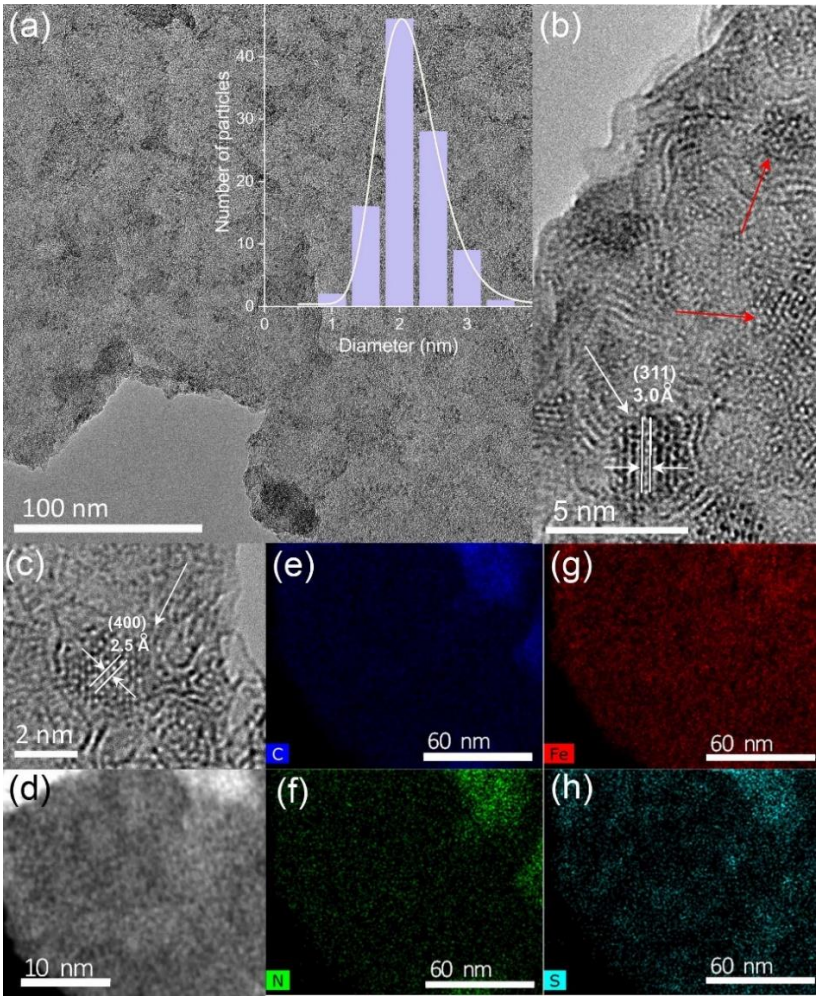

Figure 5.9. (a-c) Transmission electron micrographs of the $GCNFe_3S_4$ hybrid material. (d) High-angle annular dark-field scanning transmission electron micrographs and (e-h) corresponding elemental mapping for (e) carbon, (f) nitrogen, (g) iron, and (h) sulfur. (ref [79])

High-resolution transmission electron microscopy (HR-TEM) confirmed the presence of ultrasmall nanoparticles (**Figure 5.9 a-d**) with a mean diameter of 2.2 nm and standard deviation of 20% (inset in **figure 5.9 a**) uniformly distributed on GCN nanosheets. Further, the *d*-spacing of the lattice fringes visible in **figure 5.9 b**, **c** are 2.5 Å and 3.0 Å, which correspond to the (400) and (311) crystal plane of greigite, respectively, confirming the presence of greigite nanoparticles.[80] High-angular dark-field scanning transmission electron microscopy (HAADF-STEM,

figure 5.9 d) indicated uniform coverage of bright spots corresponding to metal-rich (*i.e.* iron from greigite) areas. Further, the elemental mapping *via* energy-dispersive X-ray spectroscopy (EDX) confirmed the homogeneous distribution of nitrogen, iron, and sulfur that are on graphene, indicating uniform functionalization of graphene with nitrile groups and greigite nanoparticles (**Figure 5.9 e-h**).

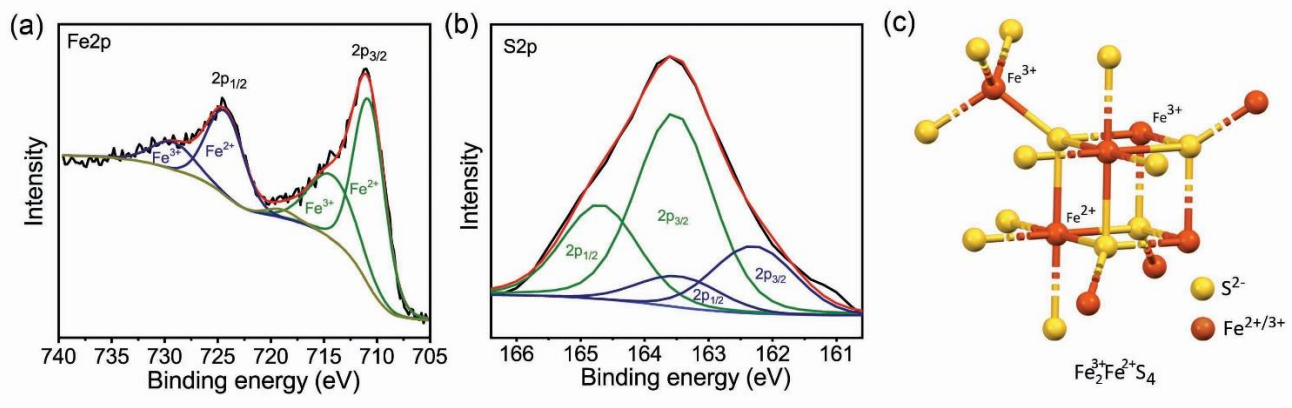

Figure 5.10. Deconvoluted X-ray photoelectron emission spectra for the (a) iron, and (b) sulfur regions. (c) The basic structural motif of greigite, corresponding to the thiocubane unit (card: amcsd 0000127). (ref [79])

The high-resolution X-ray photoelectron emission spectrum obtained for Fe2p and S2p were deconvoluted. The deconvoluted spectra of Fe2p showed (**Figure 5.10 a**) "those iron atoms were in the form of $Fe^{2+/3+}$ ions occupying the octahedral sites (at 710.7 eV representing a mixed 2.5+ valence state) and Fe^{3+} (at 724.3 eV) with a binding energy difference of 13.5 eV. These are typical for the mixed-valence spinel structure of greigite,[81] characterized by the thiocubane basic structural unit, shown in **Figure 5.10c**". Further, the $Fe^{3+}/Fe^{2+/3+}$ spectral areal ratio was observed lower (0.33) than its nominal (0.5) ratio, supporting the presence of surface defects, which was also evidenced by the irregular outer lattice fringes of the nanoparticles (**Figure 5.9 b, c**). "The spectrum of the S2p region was also deconvoluted with two pairs of doublets (**Figure 5.9b**),

reflecting the spin-orbit splitting of $S2p_{3/2}$ and $S2p_{1/2}$ peaks, separated by 1.16 eV.[82] The lower-eV doublet corresponds to S^{2-} (typical for greigite[81]), and the high-eV doublet corresponds to S_2^{2-}. The presence of these S_2^{2-} species (S^{1-}-S^{1-}) along with the increased content in Fe^{2+} is also attributed to the very small size and defect-rich structure of the nanoparticles, whereby a thermodynamically driven redox process of S^{2-} oxidation to S_2^{2-} and respective reduction of Fe^{3+} to $Fe^{2+/3+}$ (thus the lower than nominal $Fe^{3+}/Fe^{2+/3+}$ ratio) probably takes place at the exposed nanoparticles surface.[83]"

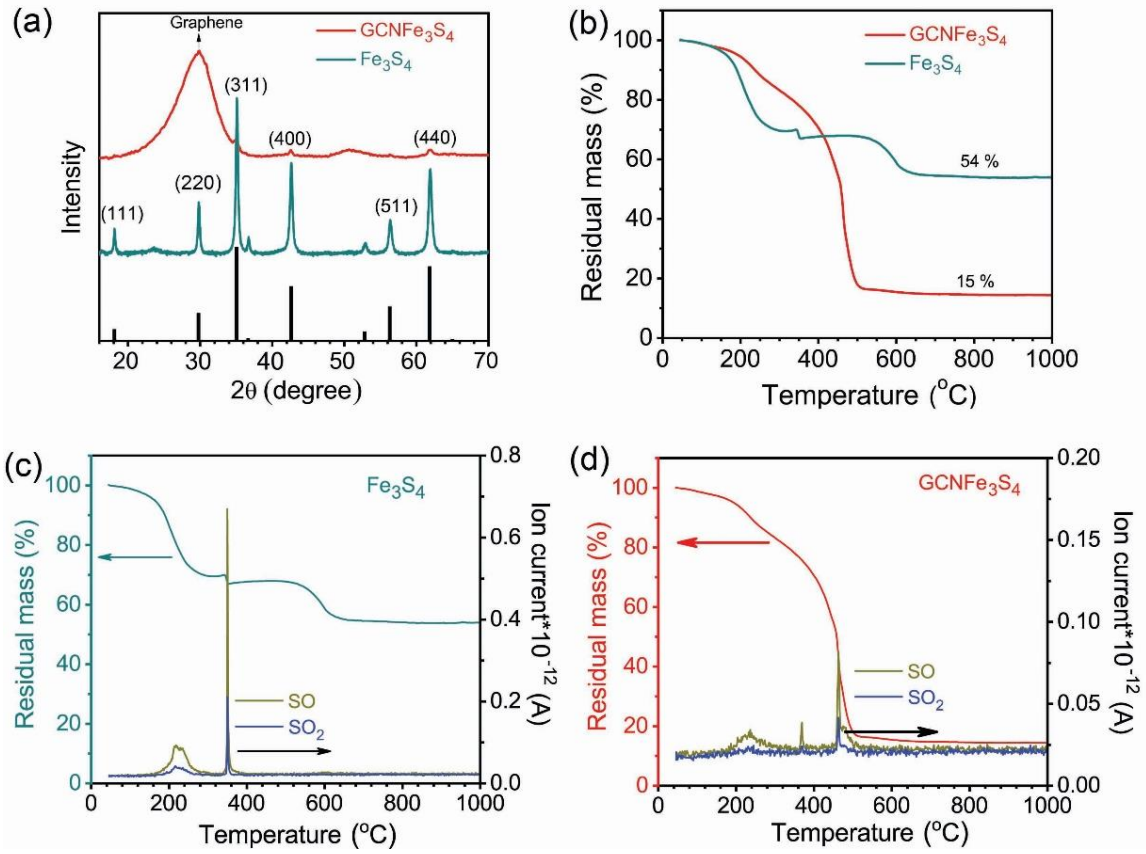

Figure 5.11. (a) X-ray diffraction (Co-Kα radiation) for $GCNFe_3S_4$ and pure Fe_3S_4. The (*hkl)* planes for Fe_3S_4 appear as bars, adopted from ICDD 04-007-9796. (b) Thermogram recorded under air for the $GCNFe_3S_4$ hybrid and pure Fe_3S_4. Thermogram and evolved gas analysis for (c) Fe_3S_4, and (d) the $GCNFe_3S_4$ hybrid. (ref [79])

The formation of Fe_3S_4 lattice was confirmed by measuring X-ray diffraction (**Figure 5.11a**) in both cases, *i.e.* in the absence and presence of the GCN during the synthesis. The (220) plane reflection was clearly visible at ca. 30^o for pure Fe_3S_4 whereas, it is hidden in the X-ray diffractogram of a hybrid due to the dominating contribution of the graphene matrix. Further, the content of Fe_3S_4 in the hybrid was obtained by thermogravimetric analysis (**Figure 5.11b**), and the content was estimated around 30 mass%. The evolved gas analysis was performed further to determine the interaction in Fe_3S_4 and GCN. The analysis showed the emission of SO and SO_2 gasses. Thus, confirming the presence of sulfur in both samples (*i.e.* in pure Fe_3S_4 and GCNFe_3S_4). In the typical analysis of pure Fe_3S_4, SO and SO_2 gasses evolved in the broad temperature range at 220-280 $^{\circ}$C, and the emissions are peaked in the short range at 345-360 $^{\circ}$C. In the GCNFe_3S_4, the SO and SO_2 emissions peaked at significantly higher temperature range (460-495 $^{\circ}$C) compare to pure Fe_3S_4, suggesting strong interaction between GCN matrix and Fe_3S_4 nanoparticles. These emissions are peaked at the same temperature where the GCN matrix decomposition takes place (i.e. the CO_2 evolution takes place upon combustion, see **appendix B, figure B1**), which supported the strong interaction achieved in the GCNFe_3S_4. "In connection to these findings, the role of GCN should be therefore highlighted, since it is endowed with a particularly high functionalization degree of 12-15%,[58] offering abundant binding sites for interacting with the in-situ grown greigite nanoparticles."

5.2.2 Electrochemical characterization

Performance in aqueous electrolyte

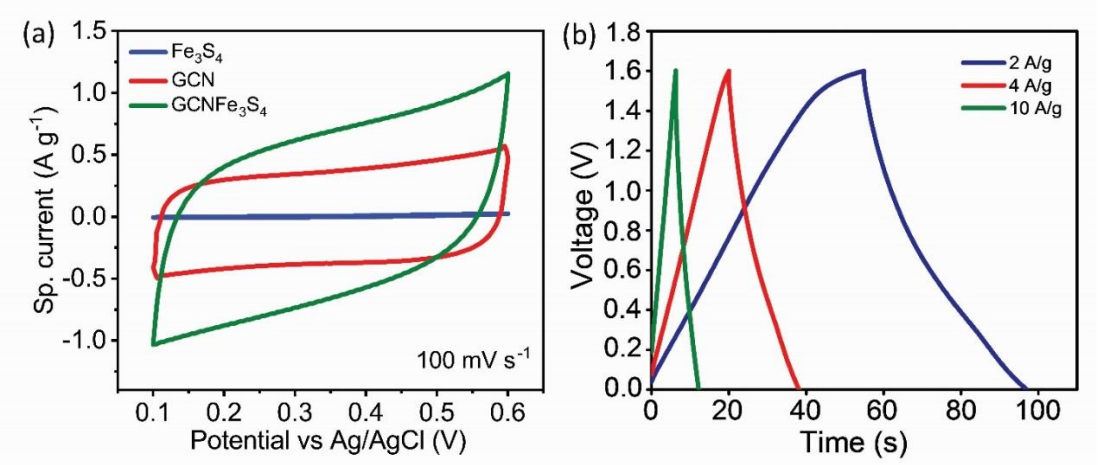

Figure 5.12. (a) Cyclic voltammograms obtained for pure Fe_3S_4, GCN, and $GCNFe_3S_4$ hybrid at a scan rate of 100 $mV{\cdot}s^{-1}$, using aqueous 1 M Na_2SO_4 in a three-electrode system, (b) galvanostatic charge-discharge curves obtained for $GCNFe_3S_4$, using 1 M KOH at different specific current. (modified figure. ref [79])

The electrochemical performance of $GCNFe_3S_4$ and its individual components GCN and greigite was first screened in a three-electrode system using aqueous electrolytes. The cyclic voltammograms obtained in 1M Na_2SO_4 electrolyte showed a large area under *i*/E curve of $GCNFe_3S_4$, indicating high capacitance than the GCN and greigite (**Figure 5.12).** Also, the cyclic voltammogram of hybrid show the slight distortion from the rectangular shape (of GCN), this can be attributed to surface redox process occur on the hybrid electrode.[84] This could be related to the presence of ultrasmall size of greigite particles and its seamless binding to the GCN support. The $GCNFe_3S_4$ was also characterized using a two-electrode system in KOH electrolyte; this electrolyte is widely used to study the performance of the transition metal sulfide to explore their redox processes. The slightly asymmetric galvanostatic charge-discharge curves attribute to the presences of reversible redox processes.

Further, in the 6 M KOH electrolyte, the capacitance of 104 F g^{-1} was achieved at specific current 1 A g^{-1} that delivered specific energy of 9.4 Wh kg^{-1} at power of 0.8 kW kg^{-1}. However, the performance is lower than the several reported values. For example, an asymmetric system of activated carbon//cobalt sulfide in-situ grown on Ni foam delivered energy of 20 Wh kg^{-1} at the power of 0.8 kW kg^{-1}. However, in these reports, the material is directly grown on the current collectors to achieve seamless contact between the active material and current collector. Thus, the performance is improved; despite, the preparation method is not suitable for large-scale production. Hence, another approach has to be incorporated to improve the performance that can bypass the production limitations.

Performance in organic electrolyte

Considering the hydrophobic nature of greigite; the performance of GCNFe_3S_4 was further explored in non-aqueous electrolytes starting with organic electrolytes. These electrolytes can provide not only the excellent solvation but also wide operating voltage range, which further improves the performance.

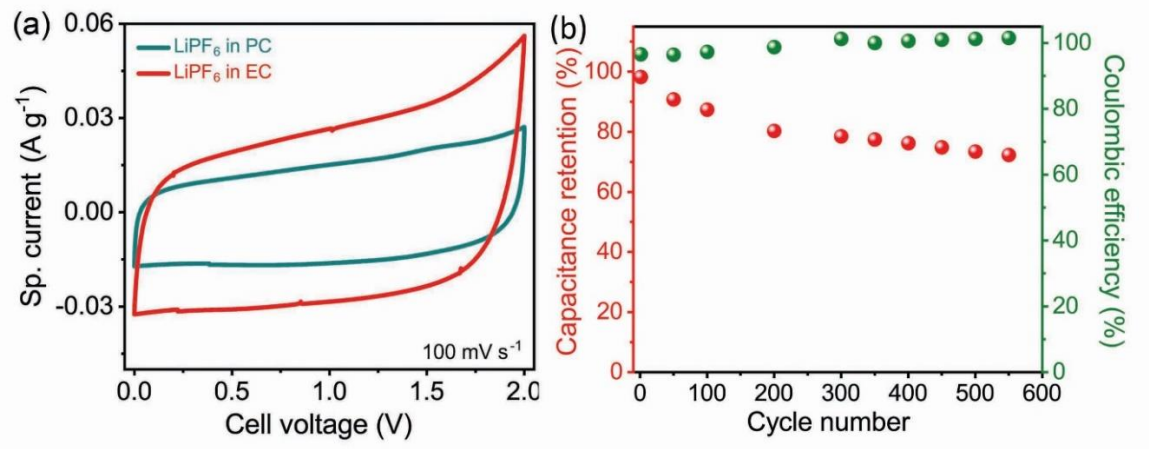

Figure 5.13. (a) Cyclic voltammograms obtained for $GCNFe_3S_4$ in an organic electrolyte with different solvents. (b) Cycling stability of the $GCNFe_3S_4$ in an organic electrolyte (1 M $LiPF_6$ in PC) at specific current 5 A g^{-1}. (modified figure. ref [79])

Thus, the $GCNFe_3S_4$ symmetric cell was screened in organic electrolytes 1 M $LiPF_6$ using different solvents such as in propylene carbonate (PC) and dimethyl carbonate: ethylene carbonate (EC) by obtaining cyclic voltammograms (**Figure 5.13**). Since the area under the cyclic voltammogram is higher for $LiPF_6$ in EC, it shows the high performance. The small ions size and high dielectric constant of EC (compare to PC) contributes to obtaining high electrochemical performance.[85,86] However, the stability of $GCNFe_3S_4$ in the organic electrolyte is inadequate (**Figure 5.13b**) because of the sulfur loss in organic solvents through the dissolution of sulfides/ polysulfides in organic solvents hence the sulfur is not available for further reaction.[87,88] Therefore, to obtain high and stable electrochemical performance, there is need of an electrolyte that can provide good solvation, wide operating voltage and will prevent the dissolution of sulfides/ polysulfides.

Performance in ionic liquids as electrolyte

Thus, the GCNFe_3S_4 symmetric cell was further characterized in the $EMIMBF_4$ ionic liquid with LiTFSI as an additive (IL+LiTFSI); this system showed a high response (**Figure 5.14a**). The cyclic voltammograms showed clear anodic and cathodic peaks with minimal voltage difference. This signifies the rapid pseudocapacitive and reversible redox process. That can be connected to the mixed valance state of greigite, containing the basic structure of thiocubane $(Fe_2^{3+}Fe_2^{2+}S_4^{2-})^{2+}$.[89] "In this unit, the oxidation states of Fe^{2+} and Fe^{3+} centers are not localized but shared among the octahedral Fe^{3+} and Fe^{2+} irons due to electron hopping, which enhances the conductivity. The mixed Fe^{2+}/Fe^{3+} valence structure is also responsible for the unique triple redox-state of the unit,[90,91] thus allowing the effective charging-discharging of two identical electrodes, from the resting $(Fe_2^{3+}Fe_2^{2+}S_4^{2-})^{2+}$ state to the oxidized $(Fe_3^{3+}Fe^{2+}S_4^{2-})^{3+}$ on the negative electrode and to the reduced $(Fe^{3+}Fe_3^{2+}S_4^{2-})^{1+}$ on the positive electrode. The X-ray photoelectron spectra of GCNFe_3S_4, after 10,000 charge-discharge cycles at 5 $A \cdot g^{-1}$, revealed only minor changes of the $Fe^{3+}/Fe^{2+/3+}$ ratio (from 0.33 to 0.48 after the cycling; **appendix B, figure B2**,), verifying the stability of the observed redox processes in the cyclic voltammograms. Nevertheless, they also showed shifts of the Fe2p X-ray photoelectron peaks and change in their widths, which along with the small $Fe^{3+}/Fe^{2+/3+}$ ratio changes, suggest that the material has not been under a redox-resting state."

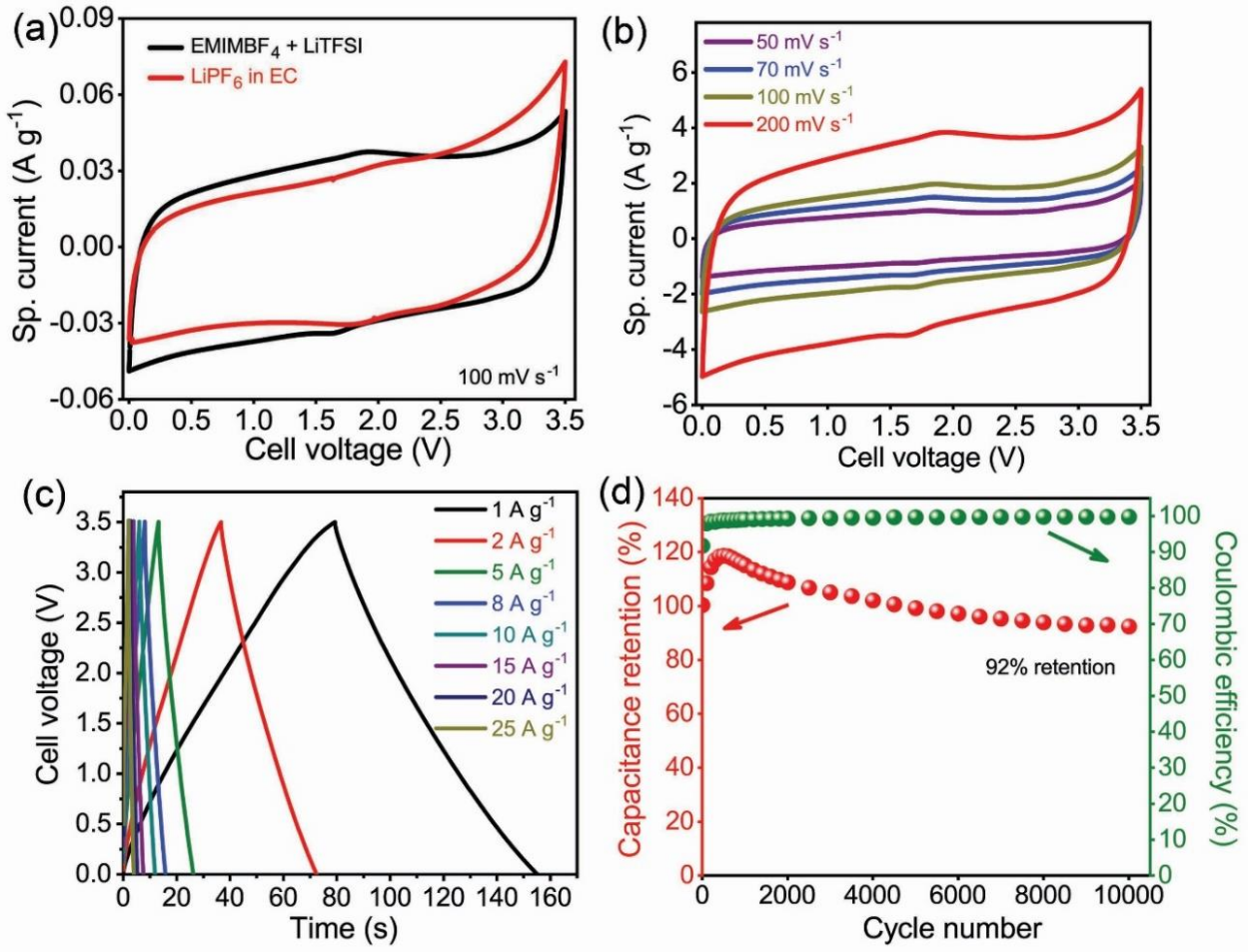

Figure 5.14.Electrochemical characterization of $GCNFe_3S_4$ symmetric cell; (a) cyclic voltammograms obtained in an organic electrolyte and ionic liquid at scan rate 100 mV s^{-1}. Electrochemical characterization of a full cell using an ionic liquid, (b) cyclic voltammograms obtained at different scan rates. (c) Galvanostatic charge-discharge curves obtained at different specific current. (d) Cycling stability and coulombic efficiency at 5 A g^{-1} after 10000 cycles. (ref [79])

The galvanostatic charge-discharge curves were symmetric and linear, also showed very small internal resistance (for example 0.04 V at 2 A g^{-1}) attributed to fast and highly reversible redox processes corroborating the observations from cyclic voltammetry results. Further, the $GCNFe_3S_4$ symmetric cell displayed outstanding cycling stability that is even after 10,000 cycles at 5 A g^{-1} the capacitance retention was 92% with coulombic efficiency around 99.8 %. The outstanding stability could

be achieved because of the prevention of the sulfur loss in IL+LiTFSI electrolyte. The interaction of $GCNFe_3S_4$ with an organic and ionic liquid electrolyte was studied by observing the dispersion of $GCNFe_3S_4$ in both electrolytes (**appendix B, figure B3a**). Where the propylene carbonate clearly develop the yellowish color after an interaction, whereas IL+LiTFSI remains the same as its original color. Further, the photoluminescence mapping was performed to probe the dissolution of sulfur in PC. The spectral changes with maximum emission at 415 nm clearly evidenced the contamination of PC (**appendix B, figure B3 b-c**). The mapping of IL+LiTFSI after interaction does not show any changes confirming the prevention of sulfur loss from the $GCNFe_3S_4$.

The specific capacitance calculated from galvanostatic charge-discharge curves was 88 F g^{-1} at specific current 5 A g^{-1} (**Figure 5.14**). Because of low internal resistance, fast and highly reversible redox process, the capacitance was retained up to 72% at 25 A g^{-1} (**Figure 5.15 a, b**). Further, **figure 5.15c** represents the comparison of rate performance of $GCNFe_3S_4$ full-cell with several reports evidenced the excellent rate capability of $GCNFe_3S_4$.

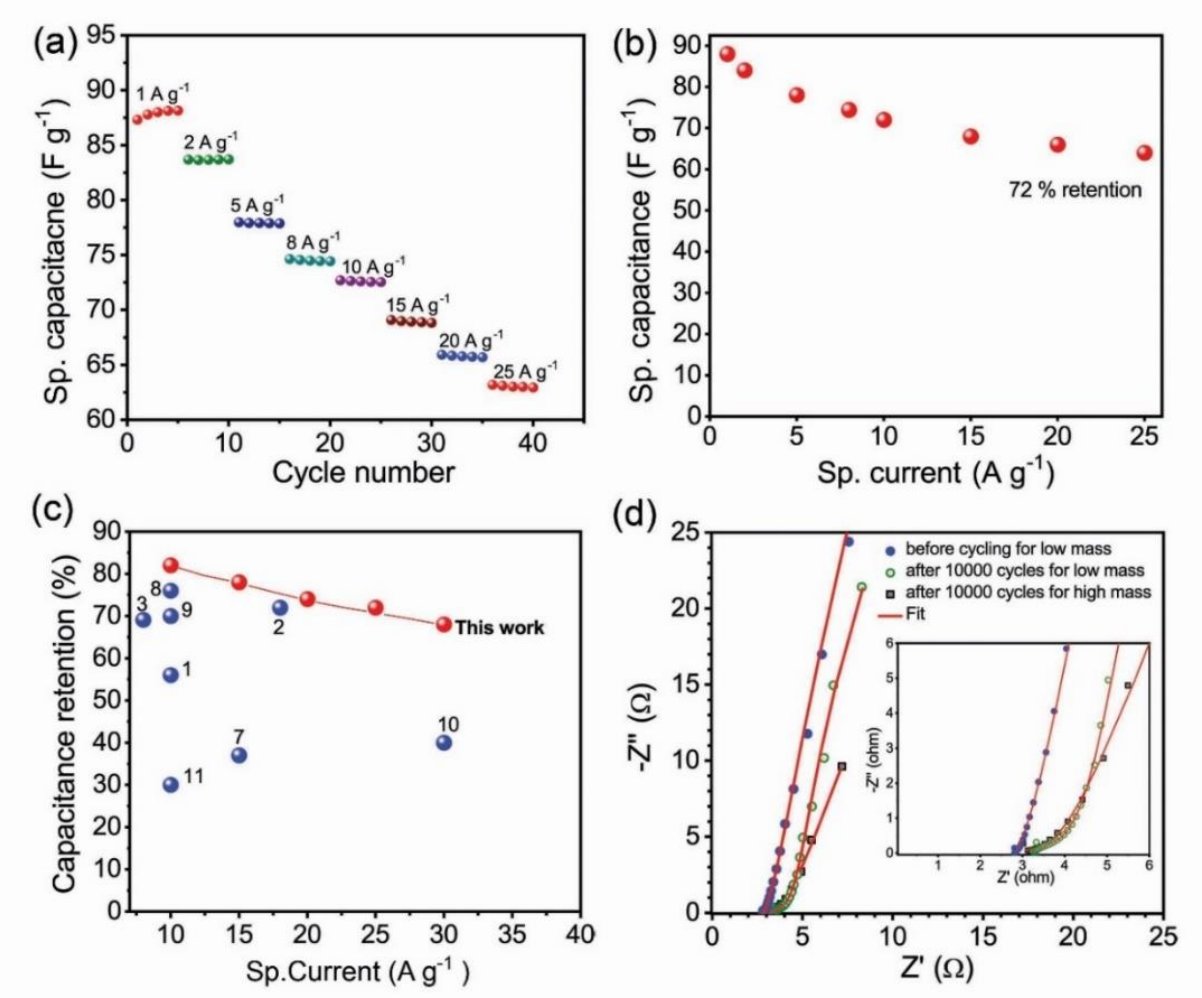

Figure 5.15. (a) Rate performance at current densities from 1 $A \cdot g^{-1}$ to 25 $A \cdot g^{-1}$. (b) Specific capacitance retention at increasing specific current. (c) Comparison of the capacitance retention of $GCNFe_3S_4$ hybrid with respect to the state-of-the-art: (1) AC//Co_9S_8-NSA,[92] (2) AC//Co_9S_8@C,[51] (3) dr-Bi_2S_3/S-NCNF//S-NCNF,[93] (7) FeS_2/GNS//$Ni(OH)_2$@Co_9S_8,[50] (8) rGO_{100}-CNT_{50}-Co_3S_4//N-doped graphene,[54] (9) $NiFeS_2$/3DSG//3DSG,[94] (10) Fe-Co-S/NF//rGO,[95] (11) $CuCo_2O_4$/CuO//RGO/Fe_2O_3.[70] (d) Electrochemical impedance spectra of the $GCNFe_3S_4$ hybrid before and after electrochemical cycling. (ref [79])

Moreover, analyzing the Nyquist plot obtained from electrochemical impedance spectroscopy supported the high rate capability and good stability. At the beginning of the high-frequency

region, the plot intersects to the real axis at a lower value, which represents low internal resistance (R_s) of 2.8 Ω before cycling. This low R_s value corresponds to low contact resistance between the electrode and current collector.[11,76] Even after 10,000 cycles, the R_s showed a minor increase to 3.3 Ω affirming the high stability of GCNFe_3S_4 symmetric cell. Further, continuing in the high-frequency region to mid-frequency region, the plot should show semicircle whose diameter anticipate the charge transfer resistance (R_{ct}). However, the absence of semicircle indicates very low resistance R_{ct} (1.18 Ω) at the electrode-electrolyte interface.[76]At the low frequencies the inclined line possess large slope indicating fast ion diffusion through the electrode.[96] Even in the high mass loading after 10,000 cycles electrodes showed low R_s and the very small reduction in slope preserving its fast charge transfer and ion diffusion through the interfaces and material respectively.

The specific capacitance obtained in the ionic liquid is 88 F g^{-1} at 1 A g^{-1} corresponded to a specific energy of 37 Wh kg^{-1} at power of 2 kW kg^{-1}. Which is significantly surpassed both energy and power (9.4 Wh kg^{-1} at 0.8 kW kg^{-1}) obtained in 6 M KOH electrolyte for same hybrid (GCNFe_3S_4). Further, the high specific energy of 25 Wh kg^{-1} is retained at a very high specific power of 35 kW kg^{-1}. Thus, it surpassed several, energy and power values reported previously, as shown in **figure 5.16a and appendix B, table B1, B2**. Further, to evaluate the GCNFe_3S_4 full cell's performance closer to the true performance metrics,[97] we analyzed the results, including the mass of the carbon-coated Al foil used as current collectors. Accordingly, the performance comparison graph changed in favor to the GCNFe_3S_4 cell (**figure 5.16b**), which were compared with the state-of-the-art in transition metal sulfides and most of the oxides, apart from the record performance of the FeOOH based system (point 14 in **figure 5.16b**). However, the production method of GCNFe_3S_4 is compatible with industrial roll-to-roll electrode coating techniques making

GCNFe$_3$S$_4$ more suitable for practical application compare to the literature examples reported in **figure 5.16**.

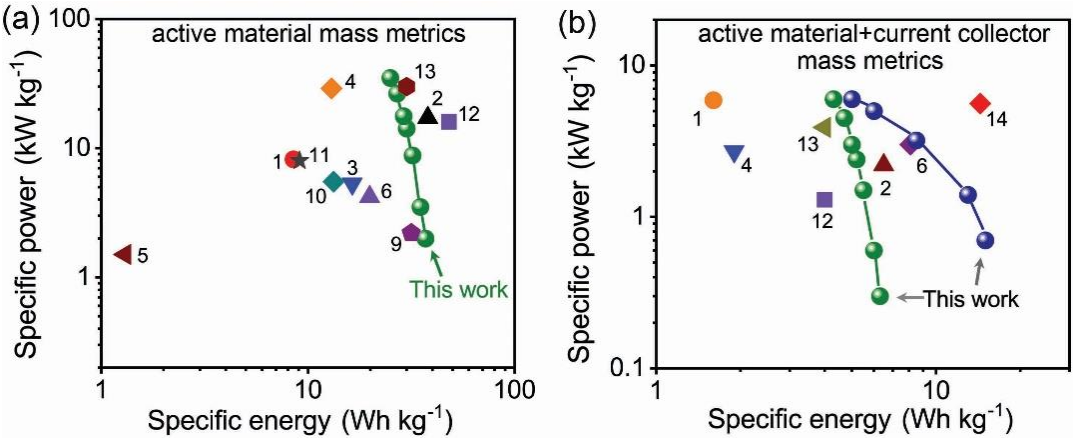

Figure 5.16. Comparison of the specific energy and power for the GCNFe$_3$S$_4$ symmetric supercapacitor with state-of-the-art full cell supercapacitors based on metal sulfides and oxides. (a) Values reported at active mass level; **[1]** AC//Co$_9$S$_8$-NSA,[92] **[2]** AC//Co$_9$S$_8$@C,[51] **[3]** Bi$_2$S$_3$/S-NCNF//S-NCNF,[93] **[4]** GCo$_{0.33}$Fe$_{0.67}$S$_2$//SG-CoNiAl,[98] **[5]** FeS$_2$//FeS$_2$,[99] **[6]** rGO/FeS//Ni(OH)$_2$,[100] **[7]** FeS$_2$/GNS//Ni(OH)$_2$@Co$_9$S$_8$,[50] **[9]** NiFeS$_2$/3DSG//3DSG,[94] **[10]** Fe-Co-S/NF//rGO,[95] **[11]** CuCo$_2$O$_4$/CuO//RGO/Fe$_2$O$_3$,[75] **[12]** Fe$_2$O$_3$-QDs-3DGF//3DHPG,[70] and **[13]** Mn$_3$O$_4$//Fe$_3$O$_4$,[101] (b) Values reported at total electrode mass level, i.e. including the mass of the current collectors (green spheres: mass loading of 0.9 mg·cm^{-2}; blue spheres: 3.5 mg·cm^{-2}); **[14]** FeOOH//NiMoO$_4$.[52] (ref [79])

Along with the production method, the areal and volumetric performance is also very important for practical applications.[57,102] Therefore, at active material loading of 3.5 mg cm^{-2} (thickness 48 µm), the GCNFe$_3$S$_4$ hybrid displayed a very high energy density of 49 mWh·cm^{-3} at a very high power density 2.4 W·cm^{-3}, that could retain up to 28 mWh·cm^{-3} at a power of 11 W·cm^{-3}. "This volumetric performance is dramatically higher compared to the previously reported TMS-based supercapacitor cells of AC//Cu$_2$O–Cu$_{1.8}$S (Ref. [103] with 2.1 mWh·cm^{-3} at 0.031 W·cm^{-3}), and AC//HTMC-SCS-M (Ref. [104] with 3 mWh·cm^{-3} at 0.77 mW·cm^{-3}). Regarding these volumetric

characteristics, the present system surpassed many more top-rated materials, not only from the family of TMS. These include metal-like fluorine-doped β-FeOOH nanorods[105] and even some of the best carbon materials operating in high potential windows such as carbon nanotubes with 47 mWh·cm^{-3} at 1.4 W·cm^{-3} (Ref. [106], using Pt mesh current collectors for boosting performance); doped carbon nanosheets with 42 mWh·cm^{-3} at 0.4 W·cm^{-3} (Ref. [107]); pillared graphene with 19.5 mWh·cm^{-3} at 9 W·cm^{-3} (Ref. [108]); dense graphene networks with 43 mWh·cm^{-3} at 7.6 W·cm^{-3} (Ref. [109]); and vertically aligned graphene sheets 6.5 mWh·cm^{-3} at 2 W·cm^{-3} (Ref.[110]). It is also indicative that the coconut-shell derived commercial activated carbon for supercapacitors (YP- 80F), displays a performance of 15 mWh·cm^{-3} at 4.1 W·cm^{-3}.[109]"

Thus, a seamless hybrid of highly functionalized graphene and ultrasmall greigite nanoparticles was achieved by a rapid, one-step synthesis method, which can take advantage of the hydrophobic nature of greigite, and triple-redox state of greigite to accomplish fast and reversible redox processes to achieve high rate capability and stability in ionic liquid electrolytes. Therefore, the hybrid can operate in a high voltage range to improve the energy and power densities.

CHAPTER 6
CONCLUSION

The goal of this doctoral dissertation was to develop and study 2D hybrids composed of transition metal oxides and sulfides for energy storage devices, particularly as electrodes for supercapacitors, in order to explore pathways for improving the performance in comparison to the current state of the art. The major challenge was to immobilize the inorganic nanoparticles firmly without the use of techniques that require treatment of the current collectors such as electrodeposition of inorganic nanoparticles on the current collector). At the same time, this must be achieved keeping a seamless structure, (as in electrodeposition) to secure electronic communication between the inorganic nanoparticles and the conductive graphene substrate. Another challenge was to observe the operation of the new electrode materials in non-aqueous electrolytes that may widen the potential window and thus boost the energy content.

The challenge of developing seamless hybrids without using complicated synthetic routes was tackled by using a highly factionalized and conductive graphene derivative (GCN) to immobilize inorganic nanoparticles via facile, one-pot microwave-assisted synthesis method. Through this, paste-ready 2D hybrids with ultra-small nanoparticles (~2-5 nm) and seamless structure were developed. Moreover, the hybrids showed high electronic and ionic conductivity and wettability due to the functionalized GCN and the ultrasmall inorganic nanoparticles. The high wettability and efficient ion diffusion in non-aqueous solvents were particularly advantageous because it allowed to bypass the low-potential window of water and thus reach higher energy content via widening the operating voltage. Another essential factor of non-aqueous electrolytes is their much less corrosive nature than water, thus allowing the use of commercial low areal-mass current

collectors, which further improved the energy content on device level. Thus, the seamless hybrids GCNak-2 and GCNFe_3S_4 are endowed with improved energy maintaining their power, excellent stability and good rate performance compared to the current state of the art.

REFERENCES:

1. Augustyn, V., Simon, P. & Dunn, B. Pseudocapacitive oxide materials for high-rate electrochemical energy storage. *Energy Environ. Sci.* **7**, 1597–1614 (2014).
2. Zhang, C., Lv, W., Tao, Y. & Yang, Q.-H. Towards superior volumetric performance: design and preparation of novel carbon materials for energy storage. *Energy Environ. Sci.* **8**, 1390–1403 (2015).
3. Fleischmann, S. *et al.* Pseudocapacitance: From Fundamental Understanding to High Power Energy Storage Materials. *Chem. Rev.* **14**, 6738–6782 (2020).
4. Trevor M Letcher. *Managing Global Warming*. (Elsevier, 2019). doi:10.1016/C2017-0-01028-5.
5. Paul Breeze. *Power System Energy Storage Technologies - 1st Edition*. (2018).
6. Trevor M. Letcher. *Storing Energy - 1st Edition*. (2016).
7. Goerlich, F. Advances in lithium-ion technology. *Medium* https://medium.com/@FranzGoerlich/advances-in-lithium-ion-technology-5d4f059bfada (2019).
8. Deepak Dubal Pedro Gomez-Romero. *Metal Oxides in Supercapacitors - 1st Edition*. (Elsevier, 2017).
9. Kim, B. K., Sy, S., Yu, A. & Zhang, J. Electrochemical Supercapacitors for Energy Storage and Conversion. in *Handbook of Clean Energy Systems* (ed. Yan, J.) 1–25 (John Wiley & Sons, Ltd, 2015). doi:10.1002/9781118991978.hces112.
10. Beguin, F. & Frackowiak, E. *Supercapacitors: Materials, Systems, and Applications*. (John Wiley & Sons, 2013).
11. Shao, Y. *et al.* Design and Mechanisms of Asymmetric Supercapacitors. *Chem. Rev.* **118**, 9233–9280 (2018).
12. Capacitance calculation for a parallel plate capacitor. *EMWorks* /application/capacitance-calculation-for-a-parallel-plate-capacitor.
13. Donne, S. W. General Principles of Electrochemistry. *Supercapacitors* 1–68 (2013) doi:10.1002/9783527646661.ch1.
14. Muzaffar, A., Ahamed, M. B., Deshmukh, K. & Thirumalai, J. A review on recent advances in hybrid supercapacitors: Design, fabrication and applications. *Renew. Sustain. Energy Rev.* **101**, 123–145 (2019).
15. Zhang, L. L. & Zhao, X. S. Carbon-based materials as supercapacitor electrodes. *Chem. Soc. Rev.* **38**, 2520–2531 (2009).
16. Afif, A. *et al.* Advanced materials and technologies for hybrid supercapacitors for energy storage – A review. *J. Energy Storage* **25**, 100852 (2019).
17. Ji, H. *et al.* Capacitance of carbon-based electrical double-layer capacitors. *Nat. Commun.* **5**, 1–7 (2014).
18. Inamuddin, D., Boddula, R., Ahamed, M. I. & Asiri, A. M. *Inorganic Nanomaterials for Supercapacitor Design*. (CRC Press, 2019).
19. Liu, J. *et al.* Advanced Energy Storage Devices: Basic Principles, Analytical Methods, and Rational Materials Design. *Adv. Sci.* **5**, 1700322 (2018).
20. Conway, B. E. & Gileadi, E. Kinetic theory of pseudo-capacitance and electrode reactions at appreciable surface coverage. *Trans. Faraday Soc.* **58**, 2493–2509 (1962).
21. Lim, E. *et al.* Advanced Hybrid Supercapacitor Based on a Mesoporous Niobium Pentoxide/Carbon as High-Performance Anode. *ACS Nano* **8**, 8968–8978 (2014).

22. Dubal, D. P., Ayyad, O., Ruiz, V. & Gómez-Romero, P. Hybrid energy storage: the merging of battery and supercapacitor chemistries. *Chem. Soc. Rev.* **44**, 1777–1790 (2015).
23. Na, W., Jun, J., Park, J. W., Lee, G. & Jang, J. Highly porous carbon nanofibers co-doped with fluorine and nitrogen for outstanding supercapacitor performance. *J. Mater. Chem. A* **5**, 17379–17387 (2017).
24. Zhao, N. *et al.* Simple electrodeposition of MoO3 film on carbon cloth for high-performance aqueous symmetric supercapacitors. *Chem. Eng. J.* **390**, 124477 (2020).
25. Liu, Y., Zhang, Y., Wu, X. W., Zhu, Y. S. & Wu, Y. P. 2 - Features of Design and Fabrication of Metal Oxide–Based Supercapacitors. in *Metal Oxides in Supercapacitors* (eds. Dubal, D. P. & Gomez-Romero, P.) 25–47 (Elsevier, 2017). doi:10.1016/B978-0-12-810464-4.00002-4.
26. Paleo, A. J. *et al.* Supercapacitors based on AC/MnO2 deposited onto dip-coated carbon nanofiber cotton fabric electrodes. *Energy Storage Mater.* **12**, 204–215 (2018).
27. Zhao, Y. *et al.* High-Performance Asymmetric Supercapacitors Based on Multilayer MnO2/Graphene Oxide Nanoflakes and Hierarchical Porous Carbon with Enhanced Cycling Stability. *Small* **11**, 1310–1319 (2015).
28. Choudhary, N. *et al.* Asymmetric Supercapacitor Electrodes and Devices. *Adv. Mater.* **29**, 1605336 (2017).
29. Zhang, S. & Pan, N. Supercapacitors Performance Evaluation. *Adv. Energy Mater.* **5**, 1401401 (2015).
30. Allen J. Bard, L. R. F. *Electrochemical Methods: Fundamentals and Applications, 2nd Edition | Wiley*. (2010).
31. Choi, C. *et al.* Achieving high energy density and high power density with pseudocapacitive materials. *Nat. Rev. Mater.* **5**, 5–19 (2020).
32. Wang, G., Zhang, L. & Zhang, J. A review of electrode materials for electrochemical supercapacitors. *Chem. Soc. Rev.* **41**, 797–828 (2012).
33. Liu, Y. & Peng, X. Recent advances of supercapacitors based on two-dimensional materials. *Appl. Mater. Today* **8**, 104–115 (2017).
34. Da, Y. *et al.* Engineering 2D Architectures toward High-Performance Micro-Supercapacitors. *Adv. Mater.* **31**, 1802793 (2019).
35. Bakandritsos, A., Jakubec, P., Pykal, M. & Otyepka, M. Covalently functionalized graphene as a supercapacitor electrode material. *FlatChem* **13**, 25–33 (2019).
36. Liu, C., Yu, Z., Neff, D., Zhamu, A. & Jang, B. Z. Graphene-Based Supercapacitor with an Ultrahigh Energy Density. *Nano Lett.* **10**, 4863–4868 (2010).
37. Le Fevre, L. W., Cao, J., Kinloch, I. A., Forsyth, A. J. & Dryfe, R. A. W. Systematic Comparison of Graphene Materials for Supercapacitor Electrodes. *ChemistryOpen* **8**, 418–428 (2019).
38. Ye, X. *et al.* A rapid heat pressing strategy to prepare fluffy reduced graphene oxide films with meso/macropores for high-performance supercapacitors. *Chem. Eng. J.* **361**, 1437–1450 (2019).
39. Ferris, A., Garbarino, S., Guay, D. & Pech, D. 3D RuO2 Microsupercapacitors with Remarkable Areal Energy. *Adv. Mater.* **27**, 6625–6629 (2015).
40. Li, X. *et al.* Hydrated ruthenium dioxides @ graphene based fiber supercapacitor for wearable electronics. *J. Power Sources* **440**, 227143 (2019).
41. He, Y. *et al.* Freestanding Three-Dimensional Graphene/MnO2 Composite Networks As Ultralight and Flexible Supercapacitor Electrodes. *ACS Nano* **7**, 174–182 (2013).

42. Li, J. *et al.* Porous Fe2O3 nanospheres anchored on activated carbon cloth for high-performance symmetric supercapacitors. *Nano Energy* **57**, 379–387 (2019).
43. Li, Y. *et al.* Fe2O3 Nanoneedles on Ultrafine Nickel Nanotube Arrays as Efficient Anode for High-Performance Asymmetric Supercapacitors. *Adv. Funct. Mater.* **27**, 1606728 (2017).
44. Nguyen, T. & Montemor, M. F. γ-FeOOH and amorphous Ni–Mn hydroxide on carbon nanofoam paper electrodes for hybrid supercapacitors. *J. Mater. Chem. A* **6**, 2612–2624 (2018).
45. Dai, E. *et al.* Co@Carbon and Co 3 O 4 @Carbon nanocomposites derived from a single MOF for supercapacitors. *Sci. Rep.* **7**, 12588 (2017).
46. Chodankar, N. R., Dubal, D. P., Kwon, Y. & Kim, D.-H. Direct growth of FeCo2O4 nanowire arrays on flexible stainless steel mesh for high-performance asymmetric supercapacitor. *NPG Asia Mater.* **9**, e419 (2017).
47. Zhou, F., Liu, Q., Gu, J., Zhang, W. & Zhang, D. A facile low-temperature synthesis of highly distributed and size-tunable cobalt oxide nanoparticles anchored on activated carbon for supercapacitors. *J. Power Sources* **273**, 945–953 (2015).
48. Chen, J., Xu, J., Zhou, S., Zhao, N. & Wong, C.-P. Amorphous nanostructured FeOOH and Co–Ni double hydroxides for high-performance aqueous asymmetric supercapacitors. *Nano Energy* **21**, 145–153 (2016).
49. Zhou, K. *et al.* Ultrahigh-Performance Pseudocapacitor Electrodes Based on Transition Metal Phosphide Nanosheets Array via Phosphorization: A General and Effective Approach. *Adv. Funct. Mater.* **25**, 7530–7538 (2015).
50. Sun, Z. *et al.* Rapid microwave-assisted synthesis of high-rate FeS_2 nanoparticles anchored on graphene for hybrid supercapacitors with ultrahigh energy density. *J. Mater. Chem. A* **6**, 14956–14966 (2018).
51. Sun, S. *et al.* Metal–Organic Framework Derived Honeycomb Co_9S_8@C Composites for High-Performance Supercapacitors. *Adv. Energy Mater.* **8**, 1801080 (2018).
52. Owusu, K. A. *et al.* Low-crystalline iron oxide hydroxide nanoparticle anode for high-performance supercapacitors. *Nat. Commun.* **8**, 14264 (2017).
53. Guan, C. *et al.* Iron Oxide-Decorated Carbon for Supercapacitor Anodes with Ultrahigh Energy Density and Outstanding Cycling Stability. *ACS Nano* **9**, 5198–5207 (2015).
54. Mohammadi, A. *et al.* Engineering rGO-CNT wrapped Co_3S_4 nanocomposites for high-performance asymmetric supercapacitors. *Chem. Eng. J.* **334**, 66–80 (2018).
55. Zhao, C., Shao, X., Zhang, Y. & Qian, X. Fe2O3/Reduced Graphene Oxide/Fe3O4 Composite in Situ Grown on Fe Foil for High-Performance Supercapacitors. *ACS Appl. Mater. Interfaces* **8**, 30133–30142 (2016).
56. Tang, X., Jia, R., Zhai, T. & Xia, H. Hierarchical Fe3O4@Fe2O3 Core–Shell Nanorod Arrays as High-Performance Anodes for Asymmetric Supercapacitors. *ACS Appl. Mater. Interfaces* **7**, 27518–27525 (2015).
57. Stoller, M. D. & Ruoff, R. S. Best practice methods for determining an electrode material's performance for ultracapacitors. *Energy Environ. Sci.* **3**, 1294–1301 (2010).
58. Bakandritsos, A. *et al.* Cyanographene and Graphene Acid: Emerging Derivatives Enabling High-Yield and Selective Functionalization of Graphene. *ACS Nano* **11**, 2982–2991 (2017).
59. Talande, S. V. *et al.* Densely Functionalized Cyanographene Bypasses Aqueous Electrolytes and Synthetic Limitations Toward Seamless Graphene/β-FeOOH Hybrids for Supercapacitors. *Adv. Funct. Mater.* **29**, 1906998 (2019).

60. Zhao, E. *et al.* Lithium Titanate Confined in Carbon Nanopores for Asymmetric Supercapacitors. *ACS Nano* **10**, 3977–3984 (2016).
61. Naoi, K. *et al.* Ultrafast charge–discharge characteristics of a nanosized core–shell structured LiFePO4 material for hybrid supercapacitor applications. *Energy Environ. Sci.* **9**, 2143–2151 (2016).
62. Okubo, M. *et al.* Nanosize Effect on High-Rate Li-Ion Intercalation in $LiCoO_2$ Electrode. *J. Am. Chem. Soc.* **129**, 7444–7452 (2007).
63. Liu, Y., Liu, X., Zhao, Y. & Dionysiou, D. D. Aligned α-FeOOH nanorods anchored on a graphene oxide-carbon nanotubes aerogel can serve as an effective Fenton-like oxidation catalyst. *Appl. Catal. B Environ.* **213**, 74–86 (2017).
64. Shao, P. *et al.* Morphology-tunable ultrafine metal oxide nanostructures uniformly grown on graphene and their applications in the photo-Fenton system. *Nanoscale* **7**, 14254–14263 (2015).
65. Chen, L.-F. *et al.* Metal-like fluorine-doped β-FeOOH nanorods grown on carbon cloth for scalable high-performance supercapacitors. *Nano Energy* **11**, 119–128 (2015).
66. Teng, Y. *et al.* Atomically Thin Defect-Rich Fe–Mn–O Hybrid Nanosheets as High Efficient Electrocatalyst for Water Oxidation. *Adv. Funct. Mater.* **28**, 1802463 (2018).
67. Song, X. & Boily, J.-F. Surface Hydroxyl Identity and Reactivity in Akaganéite. *J. Phys. Chem. C* **115**, 17036–17045 (2011).
68. Dormann, J. L., Fiorani, D. & Tronc, E. Magnetic Relaxation in Fine-Particle Systems. in *Advances in Chemical Physics* 283–494 (John Wiley & Sons, Ltd, 2007). doi:10.1002/9780470141571.ch4.
69. Masarapu, C., Zeng, H. F., Hung, K. H. & Wei, B. Effect of Temperature on the Capacitance of Carbon Nanotube Supercapacitors. *ACS Nano* **3**, 2199–2206 (2009).
70. Li, Y. *et al.* Facile low-temperature synthesis of hematite quantum dots anchored on a three-dimensional ultra-porous graphene-like framework as advanced anode materials for asymmetric supercapacitors. *J. Mater. Chem. A* **4**, 11247–11255 (2016).
71. Choi, J. W., Ock, I. W., Kim, K.-H., Jeong, H. M. & Kang, J. K. Synthesis of Pseudocapacitive Porous Metal Oxide Nanoclusters Anchored on Graphene for Aqueous Energy Storage Devices with High Energy Density and Long Cycling Stability along with Ultrafast Charging Capability. *Adv. Funct. Mater.* **28**, 1803695 (2018).
72. Xia, H. *et al.* Facile Synthesis of Hematite Quantum-Dot/Functionalized Graphene-Sheet Composites as Advanced Anode Materials for Asymmetric Supercapacitors. *Adv. Funct. Mater.* **25**, 627–635 (2015).
73. Zhao, J. *et al.* Porous 3D Few-Layer Graphene-like Carbon for Ultrahigh-Power Supercapacitors with Well-Defined Structure–Performance Relationship. *Adv. Mater.* **29**, 1604569 (2017).
74. Sun, H. *et al.* Three-dimensional holey-graphene/niobia composite architectures for ultrahigh-rate energy storage. *Science* **356**, 599–604 (2017).
75. Wang, Y. *et al.* Hydrothermal synthesis of $CuCo_2O_4$/CuO nanowire arrays and RGO/Fe_2O_3 composites for high-performance aqueous asymmetric supercapacitors. *J. Mater. Chem. A* **4**, 9977–9985 (2016).
76. Chandra Sekhar, S., Nagaraju, G. & Yu, J. S. High-performance pouch-type hybrid supercapacitor based on hierarchical NiO-Co_3O_4-NiO composite nanoarchitectures as an advanced electrode material. *Nano Energy* **48**, 81–92 (2018).
77. Sun, S. *et al.* Identifying pseudocapacitance of Fe 2 O 3 in an ionic liquid and its application in asymmetric supercapacitors. *J. Mater. Chem. A* **2**, 14550–14556 (2014).

78. Salanne, M. *et al.* Efficient storage mechanisms for building better supercapacitors. *Nat. Energy* **1**, 16070 (2016).
79. Talande, S. V. *et al.* Pinning ultrasmall greigite nanoparticles on graphene for effective transition-metal-sulfide supercapacitors in an ionic liquid electrolyte. *J. Mater. Chem. A* (2020) doi:10.1039/D0TA06998A.
80. Paolella, A. *et al.* Charge transport and electrochemical properties of colloidal greigite (Fe_3S_4) nanoplatelets. *Chem. Mater.* **23**, 3762–3768 (2011).
81. Zhao, X. *et al.* Deep eutectic-solvothermal synthesis of nanostructured Fe_3S_4 for electrochemical N_2fixation under ambient conditions. *Chem. Commun.* **54**, 13010–13013 (2018).
82. Gao, T. *et al.* Reversible S^0/MgS_x Redox Chemistry in a $MgTFSI_2/MgCl_2$/DME Electrolyte for Rechargeable Mg/S Batteries. *Angew. Chem. Int. Ed.* **56**, 13526–13530 (2017).
83. Igarashi, K., Yamamura, Y. & Kuwabara, T. Natural synthesis of bioactive greigite by solid–gas reactions. *Geochim. Cosmochim. Acta* **191**, 47–57 (2016).
84. Azman, N. H. N., Nazir, M. S. M. @ M., Ngee, L. H. & Sulaiman, Y. Graphene-based ternary composites for supercapacitors. *Int. J. Energy Res.* **42**, 2104–2116 (2018).
85. Pal, B., Yang, S., Ramesh, S., Thangadurai, V. & Jose, R. Electrolyte selection for supercapacitive devices: a critical review. *Nanoscale Adv.* **1**, 3807–3835 (2019).
86. You, X., Chaudhari, M., Rempe, S. & Pratt, L. R. Dielectric Properties of Ethylene Carbonate and Propylene Carbonate Using Molecular Dynamics Simulations. *ECS Meet. Abstr.* **MA2015-02**, 181 (2015).
87. Zhu, Y. *et al.* Electrospun FeS_2@carbon fiber electrode as a high energy density cathode for rechargeable lithium batteries. *ACS Nano* **10**, 1529–1538 (2016).
88. Yu, W.-J. *et al.* Synthesis and Electrochemical Lithium Storage Behavior of Carbon Nanotubes Filled with Iron Sulfide Nanoparticles. *Adv. Sci.* **3**, 1600113 (2016).
89. Roldan, A. *et al.* Bio-inspired CO_2 conversion by iron sulfide catalysts under sustainable conditions. *Chem. Commun.* **51**, 7501–7504 (2015).
90. Venkateswara Rao, P. & Holm, R. H. Synthetic Analogues of the Active Sites of Iron−Sulfur Proteins. *Chem. Rev.* **104**, 527–560 (2004).
91. Benício, D. *Bioinorganic Chemistry*. (University Science Book, Mill Valley, California, 1994).
92. Han, X., Tao, K., Wang, D. & Han, L. Design of a porous cobalt sulfide nanosheet array on Ni foam from zeolitic imidazolate frameworks as an advanced electrode for supercapacitors. *Nanoscale* **10**, 2735–2741 (2018).
93. Zong, W. *et al.* Sulfur-Deficient Bismuth Sulfide/Nitrogen-Doped Carbon Nanofibers as Advanced Free-Standing Electrode for Asymmetric Supercapacitors. *Small* **14**, 1801562 (2018).
94. Ma, T., Liu, H., Wang, Y. & Zhang, M. Rapid construction of three-dimensional sulfur doped graphene supported by $NiFeS_2$ interconnected networks as convenient electron/ion transport channels for flexible supercapacitors. *Electrochimica Acta* **309**, 1–10 (2019).
95. Le, K. *et al.* MOF-derived hierarchical core-shell hollow iron-cobalt sulfides nanoarrays on Ni foam with enhanced electrochemical properties for high energy density asymmetric supercapacitors. *Electrochimica Acta* **323**, 134826 (2019).
96. Low, Q. X. & Ho, G. W. Facile structural tuning and compositing of iron oxide-graphene anode towards enhanced supacapacitive performance. *Nano Energy* **5**, 28–35 (2014).
97. Gogotsi, Y. & Simon, P. True Performance Metrics in Electrochemical Energy Storage. *Science* **334**, 917–918 (2011).

98. Liu, W. *et al.* Ternary Transition Metal Sulfides Embedded in Graphene Nanosheets as Both the Anode and Cathode for High-Performance Asymmetric Supercapacitors. *Chem. Mater.* **30**, 1055–1068 (2018).
99. Venkateshalu, S., Goban Kumar, P., Kollu, P., Jeong, S. K. & Grace, A. N. Solvothermal synthesis and electrochemical properties of phase pure pyrite FeS_2 for supercapacitor applications. *Electrochimica Acta* **290**, 378–389 (2018).
100. Zhao, C., Shao, X., Zhu, Z., Zhao, C. & Qian, X. One-pot Hydrothermal Synthesis of RGO/FeS Composite on Fe Foil for High Performance Supercapacitors. *Electrochimica Acta* **246**, 497–506 (2017).
101. Choi, J. W., Ock, I. W., Kim, K.-H., Jeong, H. M. & Kang, J. K. Synthesis of Pseudocapacitive Porous Metal Oxide Nanoclusters Anchored on Graphene for Aqueous Energy Storage Devices with High Energy Density and Long Cycling Stability along with Ultrafast Charging Capability. *Adv. Funct. Mater.* **28**, 1803695 (2018).
102. Yu, D. *et al.* Scalable synthesis of hierarchically structured carbon nanotube–graphene fibres for capacitive energy storage. *Nat. Nanotechnol.* **9**, 555–562 (2014).
103. Esfandiar, A., Qorbani, M., Shown, I. & Dogahe, B. O. A stable and high-energy hybrid supercapacitor using porous Cu_2O–$Cu_{1.8}S$ nanowire arrays. *J. Mater. Chem. A* **8**, 1920–1928 (2020).
104. Lee, Y.-W. *et al.* Hierarchically assembled tubular shell-core-shell heterostructure of hybrid transition metal chalcogenides for high-performance supercapacitors with ultrahigh cyclability. *Nano Energy* **37**, 15–23 (2017).
105. Chen, L.-F. *et al.* Metal-like fluorine-doped β-FeOOH nanorods grown on carbon cloth for scalable high-performance supercapacitors. *Nano Energy* **11**, 119–128 (2015).
106. Izadi-Najafabadi, A. *et al.* Extracting the Full Potential of Single-Walled Carbon Nanotubes as Durable Supercapacitor Electrodes Operable at 4 V with High Power and Energy Density. *Adv. Mater.* **22**, E235–E241 (2010).
107. Hou, J., Cao, C., Idrees, F. & Ma, X. Hierarchical Porous Nitrogen-Doped Carbon Nanosheets Derived from Silk for Ultrahigh-Capacity Battery Anodes and Supercapacitors. *ACS Nano* **9**, 2556–2564 (2015).
108. Zhao, F.-G. *et al.* In situ tunable pillaring of compact and high-density graphite fluoride with pseudocapacitive diamines for supercapacitors with combined predominance in gravimetric and volumetric performances. *J. Mater. Chem. A* **7**, 3353–3365 (2019).
109. Li, P. *et al.* Packing Activated Carbons into Dense Graphene Network by Capillarity for High Volumetric Performance Supercapacitors. *Adv. Sci.* **6**, 1802355 (2019).
110. Yoon, Y. *et al.* Vertical Alignments of Graphene Sheets Spatially and Densely Piled for Fast Ion Diffusion in Compact Supercapacitors. *ACS Nano* **8**, 4580–4590 (2014).

LIST OF ACRONYMS

2D	two-dimensional
CE	coulombic efficiency
COFs	covalent organic frameworks
EC	ethylene carbonate
EDL/EDLC	electric double layer /electric double layer capacitor
EDX	energy-dispersive X-ray spectroscopy
EES	electrochemical energy storage
EIS	electrochemical impedance spectroscopy
GCD	galvanostatic charge-discharge
GCN	cyanographene
HAADF-STEM	high-angular dark-field scanning transmission electron microscopy
HR-TEM	high-resolution transmission electron microscopy
HR-XPS	high-resolution X-ray photoelectron
HSCs	hybrid supercapacitors
LIB	lithium-ion battery
MOFs	metal-organic frameworks
PC	propylene carbonate
PCs	pseudocapacitors
SAED	selected area diffraction
SC/SCs	supercapacitor/ supercapacitors
TGA	thermogravimetric analysis
TMDs	transition metal dichalcogenides

List of publications as a main author or co-authors

1. E. C. Vermisoglou, P. Jakubec, A. Bakandritsos, M. Pykal, **S. Talande**, V. Kupka, R. Zbořil and M. Otyepka: "CHEMICAL TUNING OF SPECIFIC CAPACITANCE IN FUNCTIONALIZED FLUOROGRAPHENE" *Chem. Mater*, vol. 31, 13, pp. 4698–4709, 2019.
   DOI: 10.1021/acs.chemmater.9b00655, **IF = 10.16**
   Author contribution: S. V. Talande, (named S. Talande, in the manuscript) had a contribution 10% in performing the electrochemical experiments under the guidance of P. Jakubec, which were involved in this article.
2. **S. V. Talande**, A. Bakandritsos, P. Jakubec, O. Malina, R. Zbořil and J. Tuček, "DENSELY FUNCTIONALIZED CYANOGRAPHENE BYPASSES AQUEOUS ELECTROLYTES AND SYNTHETIC LIMITATIONS TOWARD SEAMLESS GRAPHENE/B-FEOOH HYBRIDS FOR SUPERCAPACITORS" *Adv. Func. Mater*, vol. 29, iss. 51, p. 1906998, 2019.
   DOI: 10.1002/adfm.201906998, **IF = 15.62**
   Author contribution: S. V. Talande, performed all the experiments and analyses of results (except Mossbauer spectroscopy and magnetic charactorizations) under the guidance of A. Bakandritsos and J. Tuček,. P. Jakubec guided to perform electrochemical characterization. O. Malina and J. Tuček carried out the mossboure spectroscopy and magnetic characterizations. S. V. Talande wrote the first draft which were further improved by A. Bakandritsos and all co-authors.
3. **S. V. Talande**, A. Bakandritsos, L. Zdražil, P. Jakubec, E. Mohammadi, O. Tomanec, M. Otyepka, V. Presser, R. Zbořil, J. Tuček. "PINNING ULTRASMALL GREIGITE NANOPARTICLES ON GRAPHENE FOR EFFECTIVE TRANSITION-METAL-SULFIDE SUPERCAPACITORS IN AN IONIC LIQUID ELECTROLYTE" J. Mater. Chem. A (2020) **Accepted manuscript,**
   DOI:10.1039/D0TA06998A, **IF = 11.30**
   Author contribution: S. V. Talande performed all the experiments and analyses of results under the guidance of A. Bakandritsos. L. Zdražil performed photoluminasence spectroscopy. O. Tomanec performed HR-TEM measurements. V. Presser improved the electrochemical characterization and the manuscript. S. V. Talande wrote the first draft which were further improved by A. Bakandritsos and all co-authors.

Appendix A

Densely functionalized cyanographene bypasses aqueous electrolytes and synthetic limitations toward seamless graphene/β-FeOOH hybrids for supercapacitors.

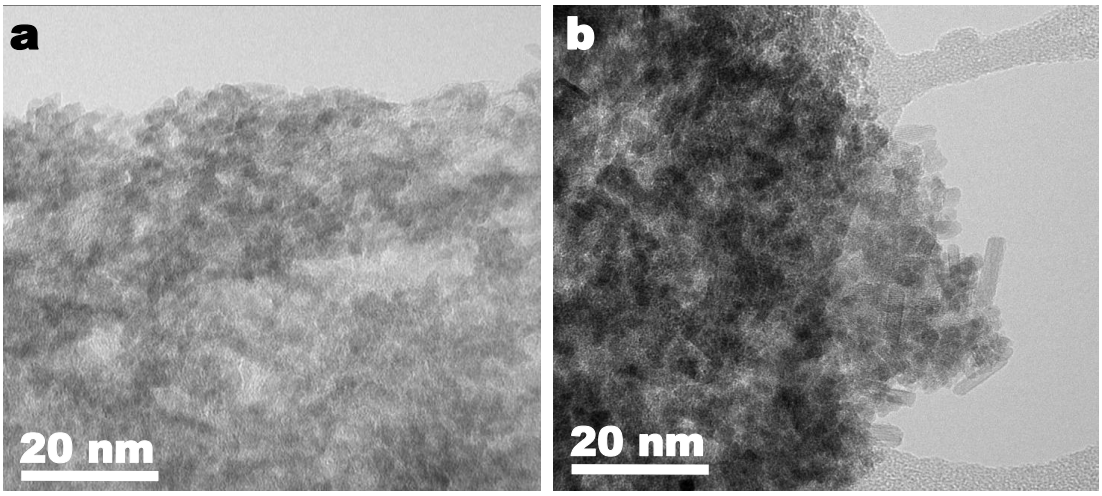

Figure A1. TEM image of **(a)** GOak-2 and **(b)** G(CN)ak-3

Table A1. Mössbauer hyperfine parameters, derived from the least-square fitting of the ^{57}Fe Mössbauer spectra of the G(CN)ak-2 and G(CN)ak-3 samples, recorded at a temperature of 5 and 300 K, where T is the temperature of the measurement, δ is the isomer shift, ΔE_Q is the quadrupole splitting, B_{hf} is the hyperfine magnetic field, and RA is the relative spectral area of individual spectral components identified upon respective spectrum fitting.

Sample	***T*** **(K)**	**Component**	$\boldsymbol{\delta}$ **± 0.01 (mm/s)**	$\boldsymbol{\Delta E_Q}$ **± 0.01 (mm/s)**	$\boldsymbol{B_{hf}}$ **± 0.3 (T)**	**RA ± 1 (%)**	**Assignment**
G(CN)ak-2	300	D1	0.35	0.52	-----	66	Fe_1 and Fe_2 sites close to Cl sites
		D2	0.35	0.94	-----	34	Fe_1 and Fe_2 sites close to Cl vacancy sites
G(CN)ak-2	5	S1	0.47	– 0.09	48.7	14	Fe_1 sites close to Cl sites
		S2	0.47	– 0.09	46.3	14	Fe_2 sites close to Cl sites
		S3	0.47	– 0.25	43.9	7	Fe_1 sites close to Cl vacancy sites
		S4	0.47	– 0.25	40.4	7	Fe_2 sites close to Cl vacancy sites
		D1	0.47	0.58	-----	8	Fe_1 and Fe_2 sites close to Cl sites
		D2	0.47	0.95	-----	4	Fe_1 and Fe_2 sites close to Cl vacancy sites
		R	0.47	-------	-----	46	Fe(III) relaxation component
G(CN)ak-3	300	D1	0.36	0.55	-----	66	Fe_1 and Fe_2 sites close to Cl sites
		D2	0.36	0.93	-----	34	Fe_1 and Fe_2 sites close to Cl vacancy sites
G(CN)ak-3	5	S1	0.46	– 0.11	48.5	15	Fe_1 sites close to Cl sites
		S2	0.46	– 0.15	46.4	15	Fe_2 sites close to Cl sites
		S3	0.46	– 0.41	45.6	8	Fe_1 sites close to Cl vacancy sites
		S4	0.46	– 0.41	42.9	8	Fe_2 sites close to Cl vacancy sites
		D1	0.46	0.39	-----	3	Fe_1 and Fe_2 sites close to Cl sites
		D2	0.46	0.79	-----	1	Fe_1 and Fe_2 sites close to Cl vacancy sites
		R	0.46	-------	-----	50	Fe(III) relaxation component

Table A2. Comparisons on the performance of supercapacitor cells (full cells only) from literature. The literature-given values apear in black text, and the recalculated values using the standard set of equations (as reported in the experimental part) for normalization and more meaningful comparisons appear in red. [***ΔV*:** operating voltage; ***C*sp(*C*m, *C*a, *C*v):** specific capacitance (gravimetric, areal, volumetric); ***I*d (*I*d,m , *I*d,a):**current density (gravimetric, areal)**; *m* (*m*a):** active material mass (areal mass); ***m*T**: total mass (mass of active material + current collectors)**; *E*(*E*m , *E*a , *E*v):** energy density (gravimetric, areal, volumetric); ***P* (*P*m , *P*a , *P*v):** power density (gravimetric, areal, volumetric); ***I*:** current; ***t*:** discharge time ;**GCD:** galvanostatic charge discharge; **CV:** cyclic voltammetry; ***T*:** temperature; **CVD:** chemical vapor deposition; **ALD:** atomic layer deposition; **HTh**: hydrothermal; **ED**: electrodeposition. The units are as reported in the header row of the table, unless otherwise stated in the specific cells; the numbers outside the brackets in the last column of the table indicate the same reference in the comparative Figure 5.8].

Anode // Cathode	*ΔV*	Given		Recalculated		Given		Recalculated		Limitations/ reported equations/ recalculation details	Ref.
		C_m	I_d	C_m	I_d	E_m	P_m	E_m	P_m		
	V	*F g*$^{-1}$	*A g*$^{-1}$	*F g*$^{-1}$	*A g*$^{-1}$	Wh kg^{-1}	kW kg^{-1}	Wh kg^{-1}	kW kg^{-1}		
Fe_3O_4@ Fe_2O_3 // Fe_3O_4@ MnO_2	2	1.49 F cm^{-3}	1.25 mA cm^{-2}	7	0.07	0.83 mWh cm^{-3}	15.6 mW cm^{-3}	3.9	0.07	3-step synthesis (HTh growth on Ti foil→high *T* treatment→ED).	1 [43]
										Equations: see comment.[1]	
		0.81 F cm^{-3}	40 mA cm^{-2}	4	2.4	0.45 mWh cm^{-3}	500 mW cm^{-3}	2.1	2.4	From the given E_v, P_v, we calculated *t* for low and high $I_{d,a}$'s, from which we calculated $I_{d,m}$, since the m_a is given (1.25 mg cm^{-2}). C_m, E_m, P_m based on m_T were recalculated including the mass of Ti foil.[2]	
Fe_2O_3/ rGO/ Fe_3O_4 // $Ni(OH)_2$	1.7	5.5	50 mA cm^{-2}	-	7.5	2.2	6.6	-	-	Thin film HTh grown on Fe foil and Ni foam, nonlinear GCD curves.	2
										Equations: see comments.[1,3]	
				0.7	0.5			0.2	5.5	With given *m*=6.4 mg and electrode area 1 cm^2, we calculated *I* (at $I_{d,a}$=50 mA cm^{-2}), from which $I_{d,m}$ was obtained (7.5 A g^{-1}) and then we calculated C_m, E_m, P_m, based on m_T.[4]	
$MnFe_2O_4$@ C // $LiMn_2O_4$	1	not given	not given	--	--	5.5	1.8	same	same	Lower E_m and P_m; Given values already based on m_T), high *T* synthesis, Ti foil as current collector.	3
										Equations: see comment.[1]	
										-	
$FeCo_2O_4$ // $FeCo_2O_4$	2.5	16.6	5 V/s	0.3	0.05	not given from GCD curves	not given from GCD curves	0.02	0.06	Lower C_m, E_m, P_m, HTh growth on Ni foam.	4
										$C=\frac{I}{m\Delta V}$; $E=\frac{C_{sp}V^2}{8}$; $P=\frac{E\,\Delta V}{V}$; ΔV is scan rate	
										Given values are based on CVs. Hence, we recalculated C_m, E_m, P_m from the given GCDs (Fig S2d), and Ni foam (3 x 2 cm^2) we obtained values	

[1] Equations used in the reference: $C_{sp} = I_d \frac{\Delta t}{\Delta V}$, $E = \frac{C_{sp}V^2}{2}$, $P = \frac{E}{t}$.

[2] Considering Ti density (4.5 g cm^{-3}) and a very thin 25 μm Ti foil (Sigma, 267503-1EA) the areal mass is obtained (7.2 mg cm^{-2}) and used for recalculations. However, probably, a thicker Ti foil was used by the authors, but there is no information given about the Ti foil characteristics.

[3] Although these equations were used by the authors, the given *E* and *P* could be reproduced only by the standard equations in the experimental part (*i.e.* containing the 3.6 factor).

[4] Considering Fe density (7.8 g/cm^3) and a very thin 1 μm Fe foil (Goodfellow, FE000050) mass is obtained (0.7 mg). For Ni foam see comment "j". Using these masses, performance values were recalculated based on m_T.

										based on m_T. (for Ni foam see comment[10] in page77)	
$ZnFe_2O_4$ /rGO // $ZnFe_2O_4$ /rGO	1.2	33.6	0.5	same	same	6.7	0.3	same	same	Lower E_m and P_m, HTh growth on Ni foam.[10] Equations are not given.[5]	5
		--	--	0.69	0.083	--	--	0.138	0.49	Given max $I_{d,m}$ is 3 A g^{-1}. Using GCD (Fig. 6b) we calculated on the 2nd row C_m, E_m, P_m, based on m_T.	
Co_3O_4@ Carbon // Co@ Carbon	1.5	17.9	1	--	--	8.8	0.375	--	--	Lower E_m and P_m, high T ; Ni Foam	6
		8.9	4	same	same	2.8	3	same	same	Equations: see comment.[1] Available data not enough for recalculation with respect to m_T, including Ni foam.	
polypyrrole -VO_x// Carbon black	1.2	92	1.5	same	same	18	0.43	same	same	Lower E_m, P_m, ED on graphite paper.	7
		--	--	31.3	2.5	--	--	6.3	1.5	Equations: see comments.[1,3]	
										Using GCD curves (Fig S6) we calculated t and the performance based on m at higher $I_{d,m}$.	
3D G/ MnO_2 // 3D G/ MnO_2	1	29.8	1.5 mA cm^{-2}	--	--	6.8	0.62	--	--	Lower E_a and P_a; 3- step synthesis (high T → CVD→ ED), Ni foam (40 mg cm^{-2}) used. Equations: see comments.[1,3]	8
		--	--	16 mF cm^{-2}	4 mA cm^{-2}	3.74	2.5	2.2 μWh cm^{-2}	2000 μW cm^{-2}	C_m is reported based on m only. Since GCD for $I_{d,a}$=1.5 mA cm^{-2} is not provided, we recalculated C_a, E_a, P_a at 4 mA cm^{-2} (provided in Fig 4d).	
Fe2O3/ rGO // MnO_2/rGO	2	--	--	18	32	10	32	--	--	900˚C, 3h for production of rGO, followed by 200˚C, 10 h treatment. High-cost Ti foils used. Equations: see comment.[5]	9 [4]
				5	8.2	--	--	2.6	8.2	From GCD curves (fig. 8b) and given E_m and P_m, t was obtained (for m_a≅2.5 mg cm^{-2} and areal mass of Ti foil[2]), thus the performance was recalculated based on m_T (2nd row).	
NiNTAS@ MnO_2 // NiNTAS@ Fe_2O_3	1.6	95.9	4	same	same	34.1	3.19	same	same	Lower C_a, E_a, P_a, 3-step synthesis of thin-film electrodes (ED on Ti foil →high T →HT). Given values are based on m only. Gravimetric performance is impractical for thin-film systems.[6] Equations: see comment [1]	10
		10 mF cm^{-2}	4	--	--	--	--	3.5 μWh cm^{-2}	329.8 μW cm^{-2}	C_a 10 mF cm^{-2} is given (Fig. 6d) corresponding to C_m=95.5 F g^{-1} at 4 A g^{-1}. Using C_m, we calculated t and then the E_a, P_a.	

[5] Even though the equations are not provided, the results were reproduced by the standard equations in the experimental part.

[6] In the case of electrode materials grown as thin-films, the m_a is limited to very low values. In this case, for example, it is 0.1 mg cm^{-2} (from given C_m=95.9 F g^{-1} and C_a=10 mF cm^{-2} (Fig 6d) at I_d=4 A g^{-1}, the m_a was directly calculated). In such systems, gravimetric performance is misleading, since higher m can be only achieved by increasing electrode area, or by increasing a lot the film thickness. Therefore, it is accepted that areal-based performance should be reported for appropriate evaluation.

FeOOH // Co–Ni double hydroxides	1.6	849 mF cm^{-2}	5 mA cm^{-2}	--	--	86.4	18.3	--	--	Lower E_m and P_m; Prepared by ED on Ni foam but given values refer to *m* only; $C_a = \frac{I}{cm^2}\frac{t}{\Delta V}$; $E_m = \frac{1}{2}\frac{\int V(t)dtI}{3.6\,m}$; $P_m = \frac{E\ 3600}{t}$	11 [46]
		353 mF cm^{-2}	50 mA cm^{-2}	2.3	0.7	22.8	11.6	0.8	0.5	C_m, E_m, P_m were recalculated based on m_T and considering the non-linear pattern of the GCD curves.[7]	
GF–CNT @Fe_2O_3 // GF–$CoMoO_4$	1.6	115.5	14			41.1	11.2	same	same	3-step synthesis on Ni foam (CVD→ high *T* → ALD), mass loading 1mg/cm^2. Equations : see comment [1,3] Ni foam was removed from the electrode architecture, but process was limitted to low mass loadings, which impractical for applications outside the area of thin film supercapacitors.	12
$CuCo_2O_4$ / CuO // RGO/ Fe_2O_3	1.6	26	10	1	0.36	9.1	8	2.1	1.8	HTh growth on Ni foam Equations: see comments.[1,3] We obtained *t* from given C_m at max. $I_{d,m}$ = 10 A g^{-1}. We calculated performance based on m_T.[8]	13 [38]
Fe_2O_3-QDs–3D GF // 3D HPG	1.6	--	20	19	2.8	--	--	6.7	2.2	HTh synthesis on carbon cloth Equations: see comment,[1] for max $P = \frac{V^2}{4mR_{ESR}}$ Given I_d is based on *m* only. From Fig. S6 we calculated *t* and the performance based on m_T.[9]	14 [39]
MnO_2/GO // Porous carbon	2	41	2	4	0.14	18.9	2	2.2	0.2	Very low P_m, since max reported I_d was limited to 2 A g^{-1} (*i.e.* low rate capability); electrodes were prepared by pasting on Ni foam. Equations: see comments.[1,3] Given values are for *m* only (7.12 mg). From GCD curves (Fig. 8a) we calculated *t* (at 2 A g^{-1}) and then the performance based on m_T.[10]	15

[7] From the given non-linear E_m=22.8 Wh kg^{-1}, we calculated the non-linear C_m=64.1F g^{-1}. From $I_{d,a}$=50 mA cm^{-2} we calculated $I_{d,m}=\frac{I}{m_a}$, since m_a is given (1.28 mg cm^{-2}/anode and 1.23 mg cm^{-2}/cathode). Using these C_m and $I_{d,m}$ we obtained the non-linear $\frac{dt}{dV}$= 3.2. With $\frac{dt}{dV}$ we calculated C_m, E_m for m_T (*i.e.* including the mass of Ni foam, a typical m_a for 80μm thick Ni foam is 34 mg cm^{-2}: www.mtixtl.com/NickelFoamforBatteryCathodeSubstrate300mmlengthx80mmwidthx0.0.aspx). From given GCD (Fig. 4) we also obtained *t* = 5.67s at $I_{d,a}$ 50 mA cm^{-2} and thus the P_m based on m_T.

[8] Given values are based on *m* only (7.6 mg cm^{-2} and 3.89 mg cm^{-2}); surface density of Ni foam (38 mg cm^{-2}) and area (2×4 cm^2) are provided. Hence total mass of Ni foam is 304 mg. Then, we replaced *m* by the total mass of electrode (*i.e.* active material + Ni foam), in order to calculate C_m for the total electrode mass.

[9] Given *m* is ~2.2 mg cm^{-2} per electrode. Carbon cloth area is 1.54 cm^2, considering the mass 13.5 mg cm^{-2} (as obtained from Fuel cell store, see for instance: http://www.fuelcellstore.com/fuel-cell-components/gas-diffusion-layers/carbon-cloth/avcarb-1071-hcb). The mass of carbon cloth is 20.3 mg per electrode. Using, GCD (Fig. S6) we obtained *t*, *I* at $I_{d,m}$ 20 A g^{-1}.

[10] Since Ni foam was used in this work to prepare the electrodes, we recalculated the performance including the mass of Ni foam. A typical value for 80 μm thick Ni foam is 34 mg cm^{-2} (as obtained from MTI Corporation, see for instance: (http://www.mtixtl.com/NickelFoamforBatteryCathodeSubstrate300mmlengthx80mmwidthx0.0.aspx). Current (*I*) was first calculated from $C_m = \frac{I}{m}\frac{\Delta t}{\Delta V}$, since C_m, *m*, Δt, ΔV are known. Then, we replaced *m* by the total mass of electrode (*i.e.* active material + Ni foam), in order to calculate C_m for the total electrode mass.

NiO NSAs@ Co_3O_4-NiO FTNs // AC@NF	1.6	623.5 mF cm^{-2}	2 mA cm^{-2}	4	0.013	216.1 μWh cm^{-2}	1580 μW cm^{-2}	1.5	0.01	3-step synthesis (HTh grown on Ni foam →wet chemical reaction→ high T treatment). Equations: see comments.[1, 3] From given GCD curve (Fig. 6e) at 2mA cm^{-2} we obtained *t*. The mass per electrode is given 5.8 mg cm^{-2} with area of 1 cm^2, hence *I* at $I_{d,a}$=2 mA cm^{-2} is 2 mA, from which we calculated gravimetric performance based on m_T. (for Ni foam[10])	16 **[47]**
Fe_2O_3@GNS // PANI/C-nanorods	4	41	3	2.8	0.2	62.4	8	6.2	0.4	Ni-foam current-collector (ref 8 there-in). Equations: see comments.[1,3] Given values based on *m* only (5 mg). GCD at max. $I_{d,m}$=3 A g^{-1} is not given, hence *t* was calculated from the given C_m. Finally, performance based on m_T was recalculated.[11]	17
FeOOH // $NiMoO_4$	1.7		10		11.3	12.7	4.9	14.4	5.6	Use of carbon cloth, HTh & electrochemical treatment for obtaining the active FeOOH phase, HTh growth of $NiMoO_4$ on Ni foam Equations: see comment.[1] Given values are based on full device mass. We recalculated the performance based on m_T.[12]	18
Porous Mn_3O_4// Fe_3O_4	2	54	30	6.3	3.5	30	30	3.5	3.5	Use of Ni foam and carbon cloth. HTh synthesis Equations: see comment.[1] Given values based on *m* only (12.5mg). We recalculated performance based on m_T.[13]	19 **[40]**

[11] The electrode area of the 2032 coin cell is 2 cm^2. For performance based on m_T and Ni areal mass see comment.[j]

[12] The given values correspond to high mass loading (24.5 mg) and reported in Figure S13b of this reference. Our recalculation was done excluding the mass of the membrane separator (given in the peer review file; response to comment F from reviewer#1).

[13] Using reported values for $I_{d,m}$, C_m and *m* we calculated *t* and then current, *I*. From these values the performance based on m_T was possible to recalculate considering one electrode with carbon cloth and the other with Ni foam (for mass of carbon cloth and Ni foam see also comment.[i,j])

Table A3. Comparisons on the performance of supercapacitor full cells (two-electrode set-ups only) for the G(CN)ak-2 hybrid in 1 M Na_2SO_4 in H_2O and 1M $LiPF_6$ in propylene carbonate. The equations dedscribed in the experimental part of the main text were used.

Anode // Cathode		**Given**				**Given**				**Limitations/ reported equations/ recalculation details**	
	ΔV	***C_m***	***I_d***			***E_m***	***P_m***				
	V	*F g^{-1}*	*A g^{-1}*			Wh kg^{-1}	kW kg^{-1}				
1M Na_2SO_4 in water											
G(CN)ak-2 // G(CN)ak-2	1.7	20	5			8	4.2			Based on active mass (2 mg)	**Our results.**
		20	10			7.8	8.5				
		0.08	0.04			0.03	0.03			Based on total electrode mass. Corresponds to $I_{d,m}$ 10 A/g	
		17 mF cm^{-2}	8.8 mA cm^{-2}			6.9 µWh cm^{-2}	7.5 mW cm^{-2}			Corresponds to $I_{d,m}$ 5 A/g	
		6 F cm^{-3}	2.2 mA cm^{-2}			2.4 mWh cm^{-3}	604.3 mW cm^{-3}			Based on active material volume Corresponds to $I_{d,m}$ 5 A/g	
		15	10			6.1	8.5			At mass loading (7.1 mg)	
		52 mF cm^{-2}	7.9 mA cm^{-2}			20.9 µWh cm^{-2}	6.7 mW cm^{-2}				
		0.7	0.4			0.3	0.4			Based on total electrode mass, including Ni foam as current collector and 7.1 mg of active material. (for $I_{d,m}$ =10 A/g)	
$LiPF_6$ in propylene carbonate											
G(CN)ak-2 // G(CN)ak-2	**3.5**	21	1.5			34.9	2.6			Based on mass loading of 14.4 mg, without current collectors.	**Our results.**
		12	5			20	8.7				
		8	7			13.3	12.2				
		3	**2.9**			**5.2**	**5**			Based on total electrode mass including Al foil with mass of 11 mg per electrode. Values corresponds to $I_{d,m}$ of 7 A/g	
		74.4 mF cm^{-2}	**31.7 mA cm^{-2}**			**126.6** µWh cm^{-2}	**55.5** mW cm^{-2}			Corresponds to $I_{d,m}$ 5 A/g	
		3.1 F cm^{-3}	**31.7** mA cm^{-2}			**5.3** mWh cm^{-3}	**2.3** W cm^{-3}			Based on total electrode volume Corresponds to $I_{d,m}$ 5 A/g	

References:

1 X. Tang, R. Jia, T. Zhai and H. Xia, *ACS Appl. Mater. Interfaces*, 2015, **7**, 27518–27525.
2 C. Zhao, X. Shao, Y. Zhang and X. Qian, *ACS Appl. Mater. Interfaces*, 2016, **8**, 30133–30142.
3 Y.-P. Lin and N.-L. Wu, *J. Power Sources*, 2011, **196**, 851–854.
4 S. G. Mohamed, C.-J. Chen, C. K. Chen, S.-F. Hu and R.-S. Liu, *ACS Appl. Mater. Interfaces*, 2014, **6**, 22701–22708.
5 S. Yang, Z. Han, J. Sun, X. Yang, X. Hu, C. Li and B. Cao, *Electrochimica Acta*, 2018, **268**, 20–26.
6 E. Dai, J. Xu, J. Qiu, S. Liu, P. Chen and Y. Liu, *Sci. Rep.*, 2017, **7**, 12588.
7 E. Karaca, K. Pekmez and N. Ö. Pekmez, *Electrochimica Acta*, 2018, **273**, 379–391.
8 Y. He, W. Chen, X. Li, Z. Zhang, J. Fu, C. Zhao and E. Xie, *ACS Nano*, 2013, **7**, 174–182.
9 H. Xia, C. Hong, B. Li, B. Zhao, Z. Lin, M. Zheng, S. V. Savilov and S. M. Aldoshin, *Adv. Funct. Mater.*, 2015, **25**, 627–635.
10 Y. Li, J. Xu, T. Feng, Q. Yao, J. Xie and H. Xia, *Adv. Funct. Mater.*, 2017, **27**, 1606728.
11 J. Chen, J. Xu, S. Zhou, N. Zhao and C.-P. Wong, *Nano Energy*, 2016, **21**, 145–153.
12 C. Guan, J. Liu, Y. Wang, L. Mao, Z. Fan, Z. Shen, H. Zhang and J. Wang, *ACS Nano*, 2015, **9**, 5198–5207.
13 Y. Wang, C. Shen, L. Niu, R. Li, H. Guo, Y. Shi, C. Li, X. Liu and Y. Gong, *J. Mater. Chem. A*, 2016, **4**, 9977–9985.
14 Y. Li, H. Zhang, S. Wang, Y. Lin, Y. Chen, Z. Shi, N. Li, W. Wang and Z. Guo, *J. Mater. Chem. A*, 2016, **4**, 11247–11255.
15 Y. Zhao, W. Ran, J. He, Y. Huang, Z. Liu, W. Liu, Y. Tang, L. Zhang, D. Gao and F. Gao, *Small*, 2015, **11**, 1310–1319.
16 S. Chandra Sekhar, G. Nagaraju and J. S. Yu, *Nano Energy*, 2018, **48**, 81–92.
17 S. Sun, J. Lang, R. Wang, L. Kong, X. Li and X. Yan, *J. Mater. Chem. A*, 2014, **2**, 14550–14556.
18 K. A. Owusu, L. Qu, J. Li, Z. Wang, K. Zhao, C. Yang, K. M. Hercule, C. Lin, C. Shi, Q. Wei, L. Zhou and L. Mai, *Nat. Commun.*, 2017, **8**, 14264.
19 J. W. Choi, I. W. Ock, K.-H. Kim, H. M. Jeong and J. K. Kang, *Adv. Funct. Mater.*, 2018, **28**, 1803695.

Appendix B

Pinning ultrasmall greigite nanoparticles on graphene for effective transition-metal-sulfide supercapacitors in an ionic liquid electrolyte

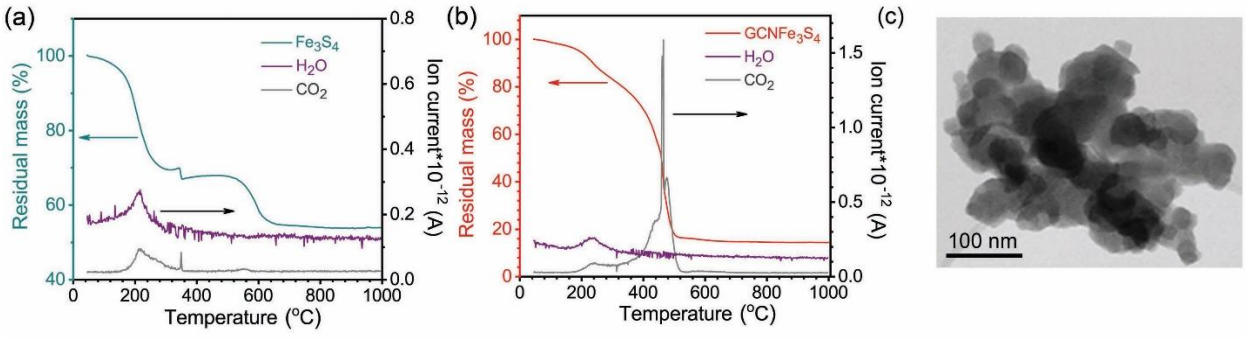

Figure B1. (a) Thermogram and (b) evolved gas analysis under air for Fe_3S_4 and $GCNFe_3S_4$ hybrid (c) TEM image of bare Fe_3S_4.

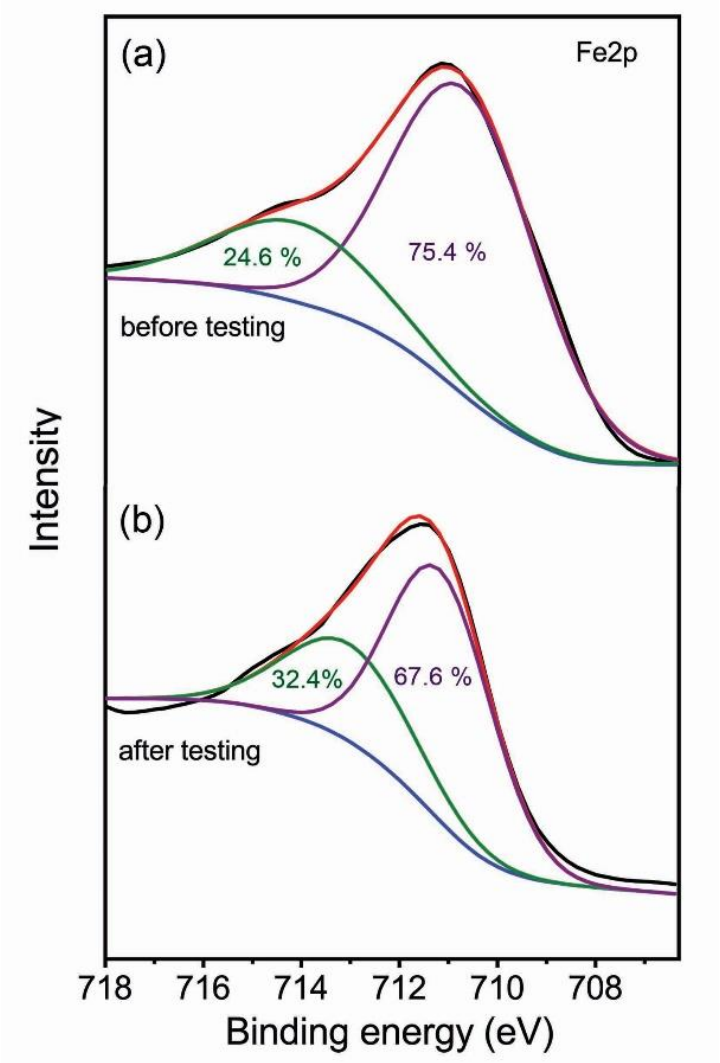

Figure B2. X-ray photoelectron emission spectra for the Fe region with deconvoluted components indicating areal% for Fe^{3+} and $Fe^{2+/3+}$ (a) before and (b) after electrochemical cycling.

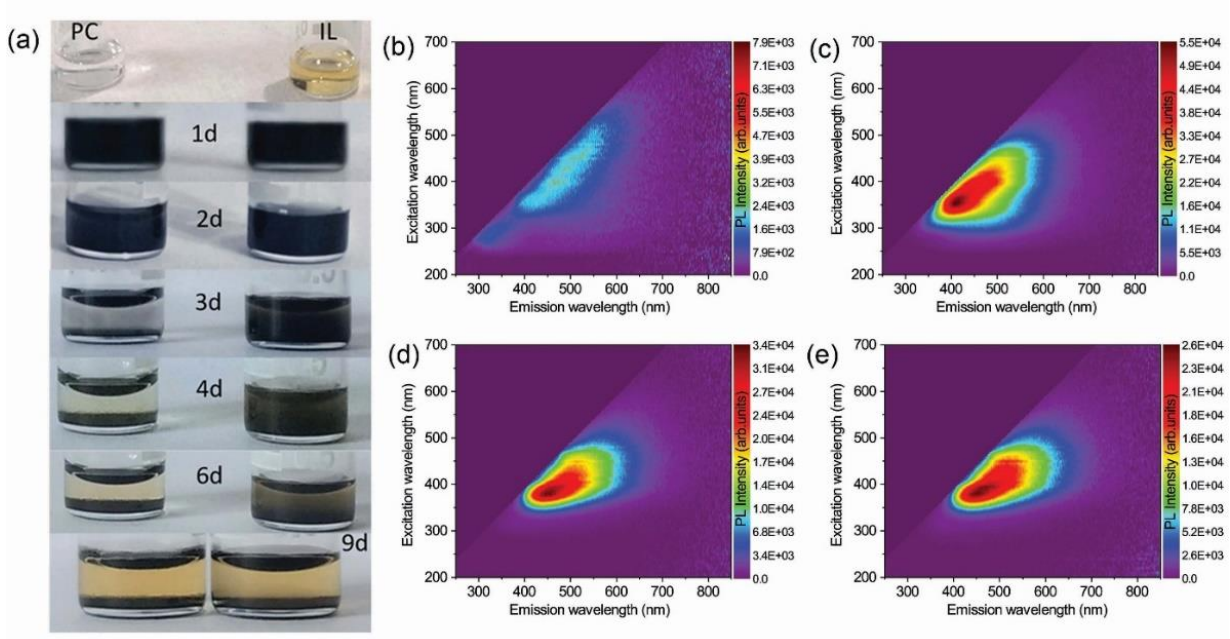

Figure B3 (a) Stability of $GCNFe_3S_4$ in organic electrolyte ($LiPF_6$ in propylene carbonate, PC) and IL+ LiTFSI electrolyte photoluminescence (PL) map of (b) pure $LiPF_6$ in PC (c) $LiPF_6$ in PC after 9 days (9d) interaction with $GCNFe_3S_4$, (d) pure IL+ LiTFSI, and (e) IL+ Li- salt after 9 d (days) interaction with $GCNFe_3S_4$.

Table B1. Comparisons of supercapacitors (full-cells only) from literature. The literature-given values appear in black. The recalculated values include the mass of the current collectors (note [1]). [***ΔV*:** operating cell-voltage; ***I*:** specific current**;** ***m*** active material mass; m_T: total mass (mass of active material + current collectors)**;** ***E*:** specific energy; ***P*:** specific power; ***C***: capacitance; ***t*:** discharge time; **MW:** microwave; **HT**: hydrothermal. The units are as reported in the header row of the table unless otherwise stated in the specific cells.]

	Anode// Cathode		Given	Recal cu-lated	Given		Recalculated		*C%* retention *vs I*	*C%* retention *vs* cycling	Electrolyte/ synthesis methods /current collectors/ recalculation details	Ref.
		ΔV	*I*	*I*	*E*	*P*	*E*	*P*				
		V	A g^{-1}	A g^{-1}	Wh kg^{-1}	kW kg^{-1}	Wh kg^{-1}	kW kg^{-1}				
1	AC//Co_9S_8 -NSA	1.7	-	-	20	0.8	-	-	54% at 10 A g^{-1}	84.4 % at 1000th cycle	1 M aq. KOH, HT growth on Ni foam (34 mg cm^{-2}).[2]	1
			5	--	8.5	8.2	1.6	0.6			Given *m* = 2.8 mg cm^{-2}. From Fig. 6b, *t* was calculated	
2	AC//Co_9S_8@C	1.6	1		58	1	-	-	72% at 18 A g^{-1}	86% at 10000th cycle	2 M KOH, multi-step, high temp. treatment, Ni foam	2
			5	0.8	--	--	8	0.6			Given *m* = 10//3 mg cm^{-2}. From Fig. 5b, c *t* was calculated.	
			18	2.8	38	17.2	6.5	2.2				
3	Bi_2S_3/S-NCNF// S-NCNF	1.35	8	-	16.4	5.3	-	-	69% at 8 A g^{-1}	118% at 2000th cycle	6 M KOH, multi-step synthesis, HT growth on the current collector	3
											Counter-el. mass not given	
4	$GCo_{0.33}Fe_{0.7}S_2$// SG CoNiAl	1.6	-		66.8	0.3	-	-	-	100% at 1000th cycle	3 M KOH, Ni foam, HT synthesis	4
			200 mV s^{-1}	0.3	13	29	1.9	0.3	-		Given *m* = 2.5 mg cm^{-2}. From Fig. 8c, *t* was calculated	
5	FeS_2//FeS_2	0.9	1		6.5	0.5	-	-	-	-	3.5 M KOH, Ni foil, HT synthesis	5
			3	0.1	1.5	1.3[3]	0.08	0.07	-	-	Given *m* = 1.9//1.9 mg. From Fig. 13b *t* was calculated	
6	RGO/FeS//Ni(OH)$_2$	1.8	0.02 A cm^{-2}	3.4	19.9	4.2	8.1	3	-	152% at 1000th cycle	2 M KOH, HT growth on Fe foil (of mass 0.7 mg [4])	6
			4.7 A g^{-1}						-		Given *m*=3//1.3 mg. From Fig. 9b, *t* was calculated.	

[1] Energy and power values are standardized on the two-electrode metrics, as described in the experimental part.
[2] A typical value for 80 μm thick Ni foam is 34 mg·cm^{-2} (as obtained from MTI Corporation, see: http://www.mtixtl.com/NickelFoamforBatteryCathodeSubstrate300mmlengthx80mmwidthx0.0.aspx). Current (*I*) was first calculated from $C = I{\cdot}t/m{\cdot}\Delta V$, since C_m, *m*, *t*, *ΔV* are known. Then, we replaced *m* by the total mass of electrode (*i.e.*, active material + Ni foam), to calculate *C* for the total electrode mass.
[3] Calculated *E* and *P* using Fig. 13b at *I* 3 A·g^{-1} then calculated performance at total electrode mass level.
[4] Considering Fe density (7.8 g·cm^{-3}) and a very thin 1 µm Fe foil (Goodfellow, FE000050) mass is obtained (0.7 mg).

7	FeS_2/GNS//Ni(OH)$_2$@Co_9S_8	1.7	15	-	27	12.6	-	-	37% at 15 A g^{-1} calculated	86% at 5000th cycle	2 M KOH, Ni foam, MW synthesis Solid-state supercapacitor.[5]	7
8	rGO_{100}-CNT_{50}-Co_3S_4//NG	1.6	10	1.17	34.1[6] 43.5	8 6.9	3.8	0.9	76% at 10 A g^{-1}	90% at 3000th cycle	3M KOH; HT synthesis; Ni foam m=3 mg cm^{-2} for 1st el., and mass ratio 0.54, hence mass of 2nd el. =5.55 mg cm^{-2}.[6]	8
9	$NiFeS_2$/3DSG//3DSG	1.6	10	-	31.6	2.2	-	-	70% at 10 A g^{-1}	82% at 5000th cycle	6 M KOH; MW synthesis No data given to calculate performance based on m_T.	9
10	Fe-Co-S/NF//rGO	1.6	10	--	13.3	5.5	0.8	0.5	62% at 10 A g^{-1}	90% at 5000th cycle	1 M KOH, HT growth on Ni foam (2x2 cm^2) m = 2.4//2.1 mg cm^{-2}. From Fig. 7c, t was calculated	10
11	RGO/Fe_2O_3//$CuCo_2O_4$/ CuO	1.6	10	0.36	9.1	8	0.3	0.3	30% at 10 A g^{-1}	83% at 5000th cycle	Lower performance; HT growth on Ni foam (2×4 cm^2) t was obtained from given C at max. I= 10 A g^{-1}. Given m is 7.9 mg cm^{-2} on +ve el.[7]	11
12	Fe_2O_3-QDs–3DGF //3DHPG	1.6	20	1.8	48	16	4	1.3	80% at 100 A g^{-1}	74% at 12000th cycle	Lower performance, HT synthesis on carbon cloth Given I was based on m only (2.0 mg cm^{-2}).[8]	12
13	Porous Mn_3O_4//Fe_3O_4	2	30	3.9	30	30	4	3.9	40% at 30 A g^{-1}	98% at 30000th cycle	Use of Ni foam and carbon cloth. HT synthesis Given values based on m only (2.5 mg cm^{-2}) el. area=2 cm^2 and electrode mass ratio is 1:1.5.[9]	13
14	FeOOH//$NiMoO_4$	1.7	10	11.3	12.7	4.9	14.4	5.6	22.5	10000	Use of carbon cloth, HT & electrochemical treatment for obtaining the active FeOOH phase, HT growth of $NiMoO_4$ on Ni foam	14
					7	1.8			67	80.8	Given values are based on full device mass. We recalculated the performance based on m_T.[10] Given m is 9 mg·cm^{-2} (first row) and 1.6 mg·cm^{-2} (second row).	
The FeOOH//$NiMoO_4$ system was the best performing iron oxide-based supercapacitor among the state-of-the-art, which was identified in the recent publication (Table S3 in the SI file from ref. [15])												
15	G(CN)ak2//G(CN)ak2	3.5	-	2.9	-	-	5.2	5	-	-	Given values are based on m_T	15

[5] The TMS are also showed promising energy and power densities for solid state supercapacitors, however, there rate performance needs further improvement as well the improvement on use of low mass current collector is required.

[6] t was calculated from the given capacitance value (96 F·g^{-1}) at 10 A·g^{-1}, E and P were then recalculated.

[7] Given values are based on m only (7.6 mg·cm^{-2} and 3.89 mg·cm^{-2}); areal density of Ni foam (38 mg·cm^{-2}) and area (2×4 cm^2) are provided. Hence total mass of Ni foam is 304 mg. Then, we replaced m by the total mass of electrode (i.e., active material + Ni foam), to calculate C_m for the total electrode mass.

[8] Given m is ~2.2 mg·cm^{-2} per electrode. The area of carbon cloth is 1.54 cm^2, considering the mass 13.5 mg·cm^{-2} (as obtained from Fuel cell store, see for instance: http://www.fuelcellstore.com/fuel-cell-components/gas-diffusion-layers/carbon-cloth/avcarb-1071-hcb). The mass of carbon cloth is 20.3 mg per electrode. Using, galvanostatic charge/discharge cycling (Fig. S6), we obtained t, I at $I_{d,m}$ 20 A·g^{-1}.

[9] Using reported values for I, C and m, we calculated t and then applied current I. From these values the performance based on m_T was possible to recalculate considering one electrode with carbon cloth and the other with Ni foam (for mass of carbon cloth and Ni foam see also note [2]

[10] The given values correspond to high mass loading (24.5 mg) and reported in Fig. 13b of this reference. Our recalculation was done excluding the mass of the membrane separator (given in the peer review file; response to comment F from reviewer#1).

Table B2. Energy and power densities of $GCNFe_2S_4$//$GCNFe_2S_4$ cell at different specific currents.

Active mass level	**Total electrode mass level**	**Active mass level**		**Total electrode mass level**		**Comments**
I	***I***	***E***	***P***	***E***	***P***	
A g^{-1}	A g^{-1}	Wh kg^{-1}	kW kg^{-1}	Wh kg^{-1}	kW kg^{-1}	
1	0.7	37	2	6.3	0.3	Low mass loading of 0.9 mg·cm^{-2} (total active mass is 4.2 mg)
2	1.4	35.4	3.5	6	0.6	
5	3.4	32.4	8.8	5.5	1.5	
8	5.5	30.3	14.2	5.2	2.4	
10	6.8	29.4	17.7	5	3	
15	10.2	27.3	26.5	4.7	4.5	
20	13.6	25	35.4	4.3	6	
1	0.5	35	2	17.4	0.9	High mass loading of 3.5 mg·cm^{-2} (total active mass is 15.6 mg)
		30 µWh·cm^{-2}	1.5 mW·cm^{-2}			
		49 mWh·cm^{-3}	2.4 W·cm^{-3}			
2	1.0	30	3	14.9	1.7	
5	2.5	20	8	9.9	3.8	
		28 mWh·cm^{-3}	11 W·cm^{-3}			
8	4.0	13	11	7.0	5.0	
10	5.0	10	13	5.0	7.0	

References

1 X. Han, K. Tao, D. Wang and L. Han, *Nanoscale*, 2018, **10**, 2735–2741.
2 S. Sun, J. Luo, Y. Qian, Y. Jin, Y. Liu, Y. Qiu, X. Li, C. Fang, J. Han and Y. Huang, *Adv. Energy Mater.*, 2018, **8**, 1801080.
3 W. Zong, F. Lai, G. He, J. Feng, W. Wang, R. Lian, Y.-E. Miao, G.-C. Wang, I. P. Parkin and T. Liu, *Small*, 2018, **14**, 1801562.
4 W. Liu, H. Niu, J. Yang, K. Cheng, K. Ye, K. Zhu, G. Wang, D. Cao and J. Yan, *Chem. Mater.*, 2018, **30**, 1055–1068.
5 S. Venkateshalu, P. Goban Kumar, P. Kollu, S. K. Jeong and A. N. Grace, *Electrochimica Acta*, 2018, **290**, 378–389.
6 C. Zhao, X. Shao, Z. Zhu, C. Zhao and X. Qian, *Electrochimica Acta*, 2017, **246**, 497–506.
7 Z. Sun, H. Lin, F. Zhang, X. Yang, H. Jiang, Q. Wang and F. Qu, *J. Mater. Chem. A*, 2018, **6**, 14956–14966.
8 A. Mohammadi, N. Arsalani, A. G. Tabrizi, S. E. Moosavifard, Z. Naqshbandi and L. S. Ghadimi, *Chem. Eng. J.*, 2018, **334**, 66–80.
9 T. Ma, H. Liu, Y. Wang and M. Zhang, *Electrochimica Acta*, 2019, **309**, 1–10.
10 K. Le, M. Gao, W. Liu, J. Liu, Z. Wang, F. Wang, V. Murugadoss, S. Wu, T. Ding and Z. Guo, *Electrochimica Acta*, 2019, **323**, 134826.
11 Y. Wang, C. Shen, L. Niu, R. Li, H. Guo, Y. Shi, C. Li, X. Liu and Y. Gong, *J. Mater. Chem. A*, 2016, **4**, 9977–9985.
12 Y. Li, H. Zhang, S. Wang, Y. Lin, Y. Chen, Z. Shi, N. Li, W. Wang and Z. Guo, *J. Mater. Chem. A*, 2016, **4**, 11247–11255.
13 J. W. Choi, I. W. Ock, K.-H. Kim, H. M. Jeong and J. K. Kang, *Adv. Funct. Mater.*, 2018, **28**, 1803695.
14 K. A. Owusu, L. Qu, J. Li, Z. Wang, K. Zhao, C. Yang, K. M. Hercule, C. Lin, C. Shi, Q. Wei, L. Zhou and L. Mai, *Nat. Commun.*, DOI:10.1038/ncomms14264.
15 S. V. Talande, A. Bakandritsos, P. Jakubec, O. Malina, R. Zbořil and J. Tuček, *Adv. Funct. Mater., 2019*, **29**, 1906998.